








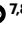





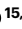




ARG1-expressing microglia show a distinct molecular signature and modulate postnatal development and function of the mouse brain

Received: 9 August 2019

Accepted: 11 April 2023

Published online: 11 May 2023

 Check for updates

Vassilis Stratoulis ^{1,2} ✉, Rocío Ruiz ³, Shigeaki Kanatani ^{4,18}, Ahmed M. Osman^{5,18}, Lily Keane^{1,18}, Jose A. Armengol ⁶, Antonio Rodríguez-Moreno ⁶, Adriana-Natalia Murgoci¹, Irene García-Domínguez ³, Isabel Alonso-Bellido³, Fernando González Ibáñez ^{7,8}, Katherine Picard ^{7,8}, Guillermo Vázquez-Cabrera^{1,3}, Mercedes Posada-Pérez^{1,3}, Nathalie Vernoux⁷, Dario Tejera⁹, Kathleen Grabert ¹, Mathilde Cheray ¹, Patricia González-Rodríguez¹, Eva M. Pérez-Villegas⁶, Irene Martínez-Gallego⁶, Alejandro Lastra-Romero⁵, David Brodin ¹⁰, Javier Avila-Cariño¹¹, Yang Cao ^{12,13}, Mikko Airavaara ^{2,14}, Per Uhlén⁴, Michael T. Heneka ^{15,16}, Marie-Ève Tremblay ^{7,8}, Klas Blomgren ^{5,17}, Jose L. Venero ^{3,19} & Bertrand Joseph ^{1,19} ✉

Molecular diversity of microglia, the resident immune cells in the CNS, is reported. Whether microglial subsets characterized by the expression of specific proteins constitute subtypes with distinct functions has not been fully elucidated. Here we describe a microglial subtype expressing the enzyme arginase-1 (ARG1; that is, ARG1⁺ microglia) that is found predominantly in the basal forebrain and ventral striatum during early postnatal mouse development. ARG1⁺ microglia are enriched in phagocytic inclusions and exhibit a distinct molecular signature, including upregulation of genes such as *ApoE*, *Clec7a*, *Igf1*, *Lgals3* and *Mgl2*, compared to ARG1⁻ microglia. Microglial-specific knockdown of *Arg1* results in deficient cholinergic innervation and impaired dendritic spine maturation in the hippocampus where cholinergic neurons project, which in turn results in impaired long-term potentiation and cognitive behavioral deficiencies in female mice. Our results expand on microglia diversity and provide insights into microglia subtype-specific functions.

Brain development begins a few weeks after conception and is thought to be complete by early adulthood. Establishment of distinct neural circuits requires the coordination of a complex set of spatial and temporal neurodevelopmental events¹. In mammals, microglia, the resident

immune cells of the CNS, populate the brain from a yolk sac origin during embryogenesis^{2–4} before the overall establishment of neural circuits. This suggests that microglia play roles in brain wiring, supported by microglia-depletion strategies during embryonic stages⁵. Likewise,

A full list of affiliations appears at the end of the paper. ✉ e-mail: vassilis.stratoulis@ki.se; bertrand.joseph@ki.se

systemic inflammation during pregnancy affects microglia and exerts deleterious effects on neuronal wiring and contributes to the etiology of neurodevelopmental and neuropsychiatric disorders⁶. Regulation of the composition of the extracellular environment, synaptogenesis, synapse pruning and myelination are all reported microglia-regulated biological processes essential to the emergence of effective neural circuits^{7,8}. Roles for microglia are also acknowledged in the context of brain diseases ranging from neurodegenerative disorders, such as Alzheimer's disease, to neoplasms, including tumors of the developing brain (that is, pediatric tumors)^{8–10}. Microglial dysfunction, including the acquisition of neurotoxic or tumor-supporting functions, is a common feature of the aforementioned brain pathologies^{9,11–13}. Hence, microglia fulfill multiple functions throughout development and under disease conditions.

Microglia are commonly regarded as a population of versatile cells that can acquire distinct phenotypes after exposure to extrinsic cues in their environment. However, recent high-throughput genome-wide sequencing data revealed that microglia with different transcriptomic profiles coexist throughout the lifespan of mice during both homeostasis and disease-related challenges^{14–19}. Whether these subsets constitute different microglial subtypes with intrinsic differences and functional specialization(s) has not been systematically explored^{18,9}. Of note, these studies show that microglia heterogeneity is strikingly high during postnatal development when the brain is expanding and establishing its neuronal networks¹. Postnatal life encompasses critical phases of mammalian brain development. Indeed, whereas the foundation of brain development begins before birth, the wiring of some neuronal networks, in particular those involved in higher cognitive and sensory functions and sex-related behaviors, takes place postnatally. During childhood and adolescence, the brain forms and refines complex neuronal networks through synaptogenesis, pruning and myelination¹. Interestingly, established microglial biological functions offer a striking match to the above-described postnatal brain developmental events⁶. Furthermore, beyond their immune functions, microglia are reported to modulate the formation of axonal tracks, synaptic reorganization and turnover and activity and contribute to the maturation of neural circuits^{5,20,21}. In addition, microglia, in particular CD11c⁺ microglia expressing large amounts of insulin-like growth factor 1, are regulators of oligodendrocyte differentiation and myelin formation²². A further emerging dimension of multifaceted microglia is that they exhibit sex differences in morphology, maturation and functional output^{23,24}, at least from postnatal development onward. Considering the plethora of functions described for microglia in the developing brain and the reported postnatal microglial transcriptional diversity, one could envisage that distinct microglial subtypes are responsible for exerting these various biological functions.

Here, we report a microglial subtype, arginase-1-expressing (ARG1⁺) microglia. ARG1⁺ microglia are morphologically indistinguishable from neighbouring ARG1⁻ microglia but can be defined by a distinct transcriptomic profile and a unique spatial and temporal distribution and exert a unique function in the developing brain.

Results

ARG1⁺ microglia are primarily found in the basal forebrain (BF)

Using an antibody screen, we identified that in wild-type (WT) and unchallenged brains of mice of both sexes, a subset of microglia co-expresses ionized calcium-binding adaptor molecule 1 (IBA1; encoded by the gene *Aif1*) and the enzyme ARG1. Immunofluorescence analysis of WT mouse brains at postnatal day 10 (P10) and P28 revealed that ARG1⁺ microglia coexist along with ARG1⁻ microglia that do not express ARG1 (Fig. 1a,b). We also identified ARG1⁺IBA1⁻ cells in the cerebellum and around the lateral ventricles, which morphologically do not resemble microglia and were therefore excluded from this study (Extended Data Fig. 1). We further confirmed the existence of ARG1⁺ microglia in YARG reporter mice²⁵, which express yellow fluorescent fusion protein (YFP)

inserted downstream of the endogenous stop codon of the *Arg1* gene (Extended Data Fig. 2a).

To gain further insights into the topographical localization of ARG1⁺ microglia, immunolabeling-enabled three-dimensional imaging of solvent-cleared organs (iDISCO+) three-dimensional (3D) deep imaging of ARG1 and IBA1 expression was performed on P10 and P28 mouse brains²⁶. ARG1⁺ microglia were found to cluster in several brain regions both at P10 and P28. The ARG1⁺ microglia located in the BF and ventral striatum (vStr) constituted the largest ARG1⁺ microglia cluster (Fig. 2a and Supplementary Videos 1–4). Further registration of the P28 ARG1⁺ microglia population against the Allen Developing Mouse Brain Atlas (<http://mouse.brain-map.org>) revealed that the highest concentration of ARG1⁺ microglia is located in the ventral pallidum, followed by adjacent areas (Fig. 2b). The BF is an area rich in cholinergic neurons that project to the hippocampus, a structure engaged in cognition²⁷, and loss of BF cholinergic projections and reduction of BF volume are associated with reduced cognitive capability²⁷.

ARG1⁺ microglia are abundant in early development

While ARG1⁺ microglia were present at all investigated ages (P10, P28 and P100), and their numbers varied greatly, ARG1⁺ microglia number in the BF/vStr was notably reduced from P10 to P28 (Fig. 1c), while at P100, only a residual population could be observed (Extended Data Fig. 2b,c). Of note, early postnatal life is a critical period for brain development, during which brain size increases and neuronal spines and networks mature, including cholinergic BF neurons²⁸. Collectively, these data support the existence of a subset of microglia in the unchallenged WT mouse brain that expresses ARG1 and exhibits intriguing spatiotemporal overlap with the cholinergic system.

ARG1⁺ microglia do not exhibit morphological aberrations

We used morphometric analysis to compare ARG1⁺ microglia to neighbouring ARG1⁻ microglia from P10 and P28 animals, but no notable morphological differences were observed (Extended Data Fig. 3a,b).

P13 ARG1⁺ microglia have a unique transcriptomic profile

To assess whether ARG1⁺ microglia are characterized by a distinct gene expression profile, we performed bulk RNA-sequencing (RNA-seq) analysis. We isolated ARG1-YFP⁺CX3CR1⁺ microglia and ARG1-YFP⁻CX3CR1⁺ microglia from the area ventral to the corpus callosum and anterior to the lateral ventricles and excluding the olfactory bulb of P13 female and male YARG animals (Fig. 3a). Confirmatory immunohistochemistry analysis in YARG mice showed that ARG1 and YFP protein expression in cells are concurrent (Extended Data Fig. 2a). Furthermore, we validated in CX3CR1-green fluorescent protein (GFP) mice, which express GFP under the control of the endogenous *Cx3cr1* locus, that a subset of CX3CR1-expressing microglia expresses ARG1 in the BF (Extended Data Fig. 4a), while in ventricles, ARG1⁺ cells that morphologically do not resemble microglia do not express CX3CR1-GFP (Extended Data Fig. 4b). We also observed in WT brain vessels ARG1⁺IBA1⁺ cells with amoeboid morphology, which were strongly reminiscent of perivascular macrophages²⁹ (Extended Data Fig. 4c). In fact, those cells were positive for the macrophage mannose receptor (CD206)²⁹, in contrast to the microglia that were negative for this marker and exhibited a ramified morphology. Based on the above observations, the cell populations of interest were collected by fluorescence-activated cell sorting (FACS) using negative CD206 selection (to exclude perivascular macrophages), positive selection for CX3CR1 (that is, microglial/myeloid marker) and ARG1-YFP expression (Fig. 3a and Extended Data Fig. 5a).

Three independent biological replicates from pooled female or male mouse brain tissues were used for transcriptomic analysis. RNA-seq data revealed that ARG1⁺ microglia possess a unique and distinct transcriptomic profile compared to ARG1⁻ microglia from the same brain area. One hundred and fifty genes were upregulated and 109 genes were downregulated at least twofold in ARG1⁺ microglia

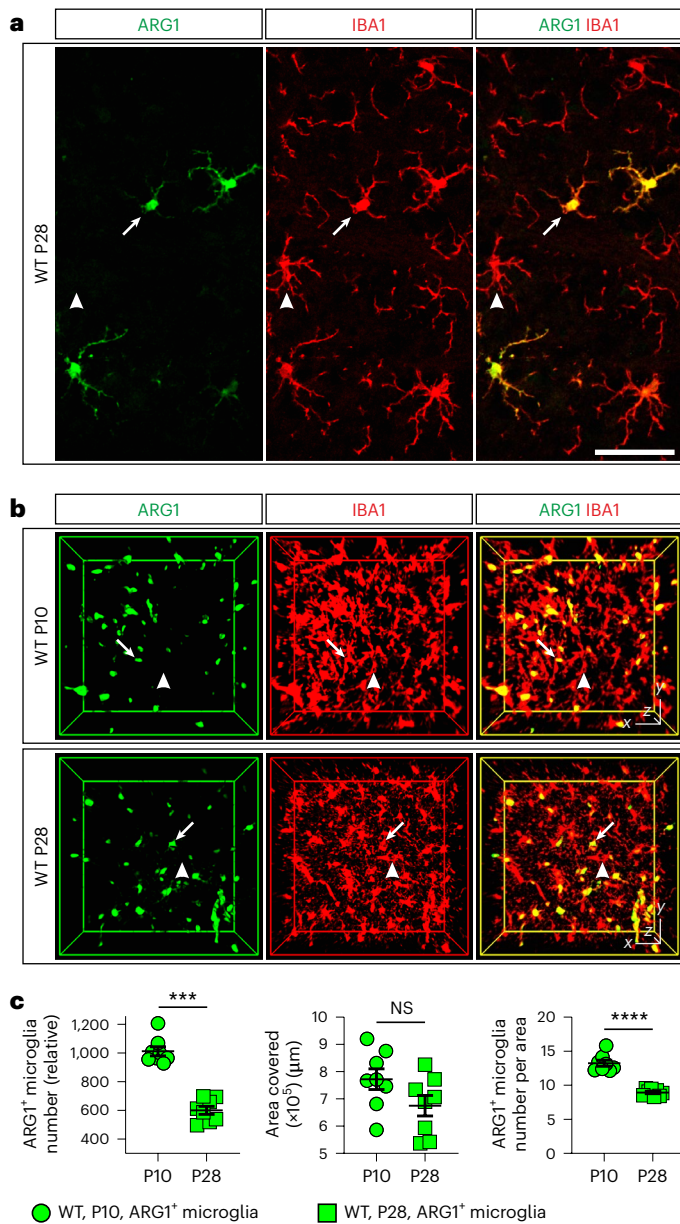


Fig. 1 | ARG1⁺ microglia coexist in the same vicinity as ARG1⁻ microglia in the BF of P10 and P28 female and male mice. a, b, ARG1⁺ microglia (arrows) and ARG1⁻ microglia (arrowheads) in WT female (a; confocal) and WT male (b; iDISCO) mouse brains. Scale bars, $x = 50 \mu\text{m}$ and $z = 8.25 \mu\text{m}$ (a) and $x = y = 50 \mu\text{m}$ and $z = 150 \mu\text{m}$ (b). **c,** The ARG1⁺ microglia population declines with age ($n = 4$ female and 4 male animals). Each circle (P10) or square (P28) corresponds to one animal; *** $P = 0.0002$, ARG1⁺ microglia number (relative); **** $P < 0.0001$, ARG1⁺ microglia number per area; NS, not significant. Data are shown as mean \pm s.e.m. Statistically significant differences were determined by unpaired two-sided t -tests (for area covered and ARG1⁺ microglia number per area) and two-sided Mann–Whitney U -test (for ARG1⁺ microglia number).

compared to in ARG1⁻ microglia (Fig. 3b,c and Supplementary Table 1). The transcriptomes of ARG1⁺ microglia from P13 females and males were almost indistinguishable and showed substantially less sex-dependent variation than ARG1⁻ microglia (Extended Data Fig. 5b). Also, the numbers of ARG1⁺ microglia in males and females were similar, as shown by unbiased stereological counting and FACS (Extended Data Fig. 6). Despite the detection of substantial microglial ARG1 (as well as YFP for YARG mice) protein expression even at P28 in the BF of unchallenged

WT and YARG mice, ARG1 transcripts were not observed in the RNA-seq analysis for P13 ARG1–YFP⁺CX3CR1⁺CD206⁻ microglia (Supplementary Table 1). However, quantitative PCR with reverse transcription (RT–qPCR) analysis performed on sorted ARG1–YFP⁺CX3CR1⁺CD206⁻ and ARG1–YFP⁻CX3CR1⁺CD206⁻ cell populations using the same extraction pipeline confirmed restriction of the expression of ARG1 gene expression to the ARG1⁺YFP⁺CX3CR1⁺CD206⁻ population (Extended Data Fig. 7a–c). ARG1⁺ microglia express high mRNA copy numbers of microglial homeostatic genes, such as *P2ry12*, *Tmem119*, *Siglech*, *Gpr34*, *Socs3*, *Hexb*, *Olfml3* and *Fcrls*³⁰, confirming that these cells are indeed microglia (Fig. 3e). Of note, most of these microglial homeostatic genes are expressed at lower levels in ARG1⁺ than in ARG1⁻ microglia from the same brain area, a feature that has been reported for reactive³¹ and disease-associated microglia^{32,33}.

Although ARG1 gene expression has been traditionally associated with the outdated term alternative microglia, our RNA-seq analysis showed that ARG1⁺ microglia cannot be classified as such (Extended Data Fig. 7d). Instead, ARG1⁺ microglia are characterized by high expression of genes such as *Axl*, *Apoe*, *Clec7a*, *Mgl2*, *Lgals3* and *Igf1* (ref. 30; Fig. 3b–d and Supplementary Table 1). Coexpression of GALECTIN-3 (encoded by the gene *Lgals3*), COLEC12 and CLEC7A proteins and *Apoe*, *Igf1*, *Lpl* and *Spp1* transcripts in ARG1⁺ microglia was further validated by immunohistochemistry and qPCR, respectively (Extended Data Figs. 7e,f and 8b,c). A recent high-throughput microglia single-cell transcriptomic analysis revealed several distinct microglial subsets¹⁷. In the context of the current investigation, Hammond et al.¹⁷ found that a particular subtype of microglial cells, defined as cluster 1, showed elevated levels of ARG1 expression at young ages. Direct comparison of the ARG1⁺ microglia from this study and cluster 1 genes¹⁷ revealed that both microglial types share a transcriptomic signature of 16 genes (with a fold change (FC) of >1.5), including upregulation of *Apoe*, *C3*, *Lgals3*, *Mgl2* and *Igf1* (Extended Data Fig. 7g).

ARG1⁺ microglia have increased numbers of cellular inclusions

Ultrastructural analysis of ARG1⁺ microglial cell bodies in the BF/vStr of female mice revealed a higher number of empty phagocytic inclusions and total number of inclusions, which considered empty and inclusions with content together, than in ARG1⁻ microglia, indicating increased phagocytic activity (Fig. 4a–c). Although there was no notable difference in the number of direct contacts between ARG1⁺ microglia and synaptic elements, some of the inclusions contained structures with synaptic vesicles, implying the phagocytosis of presynaptic axon terminals³⁴ and involvement in neural development. The proximity of ARG1⁺ microglia to cholinergic neurons was verified by immunohistochemistry (Fig. 4d).

Arg1 microglial deletion impacts cognition in female mice

Given the unique spatiotemporal distribution and substantially different transcriptomes of ARG1⁺ microglia compared to neighboring ARG1⁻ microglia, we sought to investigate if they also have a distinct functional specialization. We specifically knocked out the ARG1 gene in microglia by crossing *Cx3cr1*^{CreER} mice with *Arg1*^{fl/fl} mice and induced recombination by multiple tamoxifen injections from P1 (Fig. 5a,b). Using immunohistochemistry, we confirmed that ARG1 expression was suppressed efficiently (Extended Data Fig. 8a). Co-staining for GALECTIN-3 and CLEC7A proteins, which are coexpressed in ARG1⁺ microglia in WT mice, revealed that in ARG1-knockout animals, the number of GALECTIN-3- and CLEC7A-expressing microglia persisted in the BF at similar numbers as observed in WT littermates (Extended Data Fig. 8b,c). This implies that after ARG1 knockout, ARG1⁺ microglia stop expressing ARG1, but they do not cease to exist. Future in vivo lineage-tracing studies would certainly be informative to decipher ARG1⁺ microglia ontogeny and maturation.

The topographic organization of ARG1⁺ microglia proximal to the cholinergic nucleus of the BF, a major nucleus for cognition²⁷,

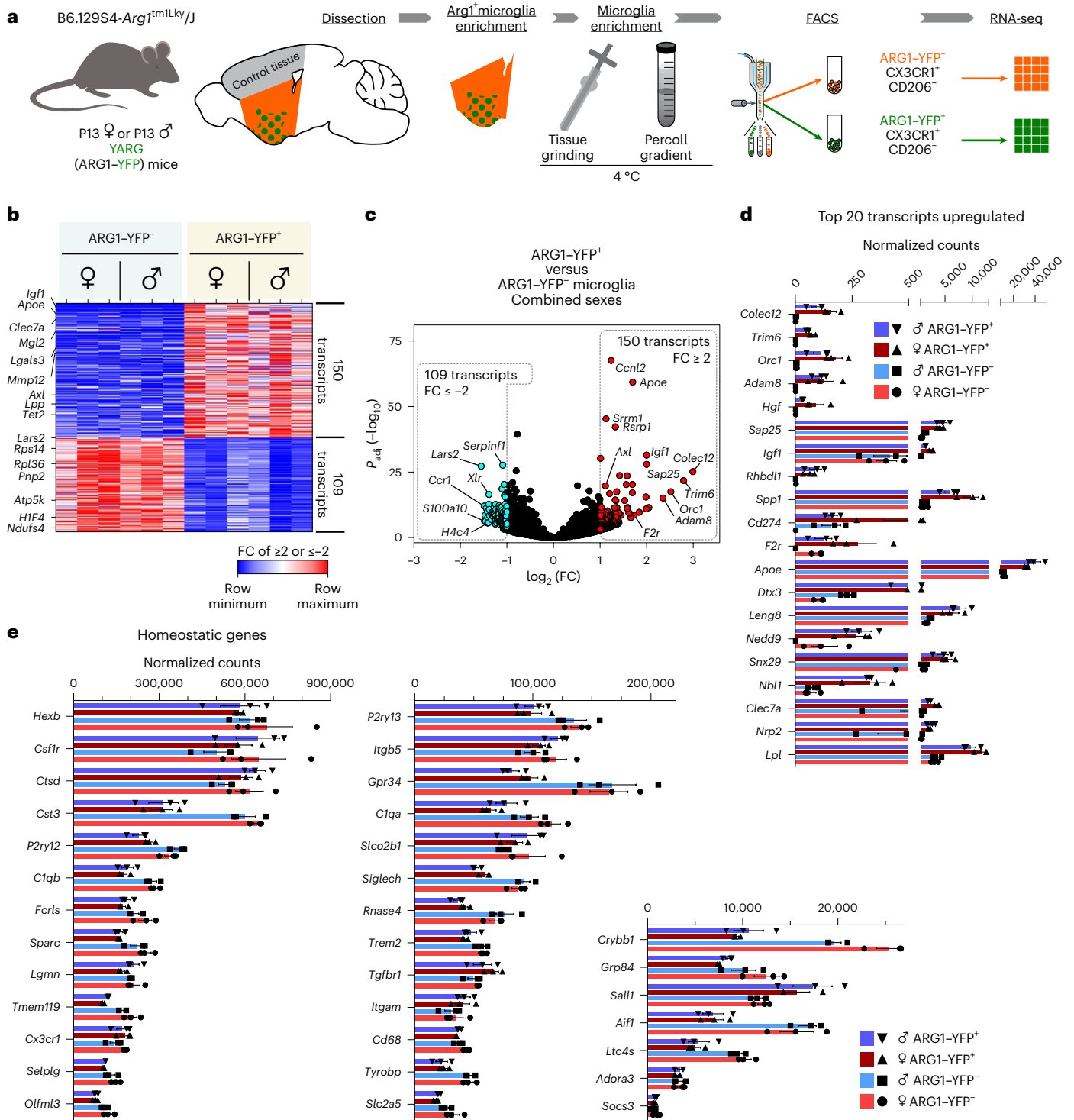


Fig. 3 | The ARG1⁺ microglia transcriptome is substantially different than that of neighboring ARG1⁻ microglia in female and male P13 mice. **a**, ARG1⁺ microglia were isolated from P13 YARG mice. Three to five brains were dissected from either female or male mice per biological replicate ($n = 3$ litters per sex). Tissues were ground on ice before performing Percoll gradient centrifugation. ARG1⁺ microglia and ARG1⁻ microglia were sorted by flow cytometry, followed by RNA-seq. **b, c**, Heat map (**b**) and volcano plot (**c**) of up- and downregulated

(at least twofold) genes in ARG1-YFP⁺ and ARG1-YFP⁻ microglia. Only validated genes are included in this list. **d**, List of the 20 most upregulated genes in ARG1-YFP⁺ microglia. **e**, ARG1-YFP⁺ (and ARG1-YFP⁻) microglia express high numbers of transcripts of homeostatic microglial genes. Data in **d** and **e** are shown as mean \pm s.e.m. P values (two sided) attained by the Wald test are corrected for multiple testing using the Benjamini-Hochberg method (P_{adj}). Statistically significant differences were not measured for **d** and **e**.

reveal differences between female and male ARG1⁺ microglia (Extended Data Fig. 8d,e). Whether the observed behavior difference between male and female mice after microglial *Arg1* knockout could be linked

to the reported regulation of ARG enzymes by steroid hormones³⁷ requires further investigation. Yet, similar sex differences have been reported when *Arg1* is depleted in peripheral myeloid cells³⁸.

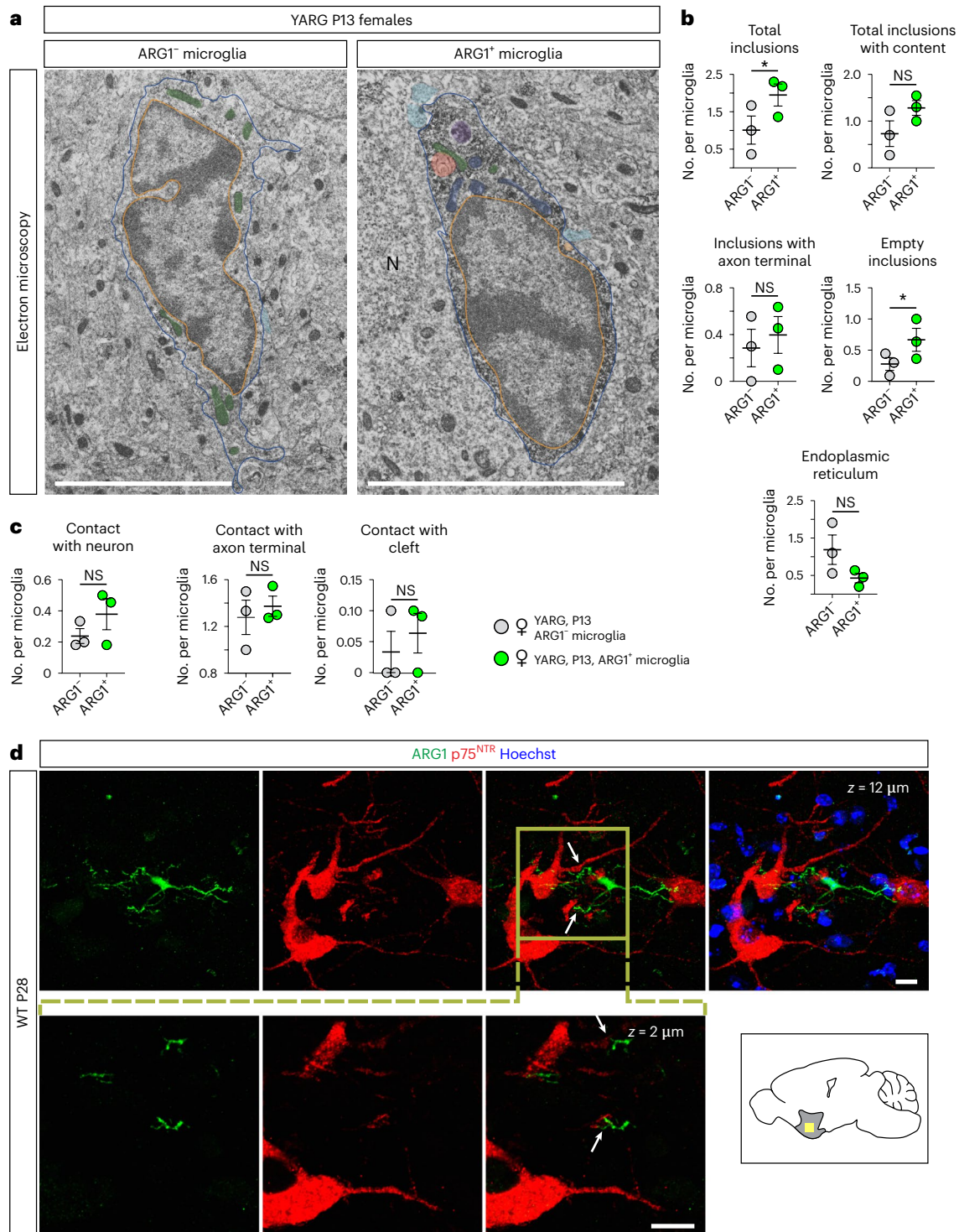


Fig. 4 | ARG1⁺ microglia contain more inclusions than ARG1⁻ microglia in the BF of P13 YARG mice. **a**, Representative transmission electron microscopy images showing the ultrastructure of ARG1⁻ and ARG1⁺ microglia from P13 YARG female brains in the BF/vStr. **b,c**, Quantitative analysis of intracellular features (**b**) and intracellular relationships (**c**; $n = 3$ female animals); total inclusions, $P = 0.0283$; empty inclusions, $P = 0.0454$. **d**, In the WT P28 BF/vStr, ARG1⁺ microglia are in close proximity to cholinergic neurons, as detected with an antibody to p75^{NTR} ($n = 3$). Scale bars, 5 μm. The yellow square indicates the location of the corresponding images

below; cyan, axon terminals; red, inclusion with content; orange, empty inclusion; green, mitochondria; blue, holy mitochondria; purple, secondary lysosome; N, neuron; asterisk, endoplasmic reticulum; blue line, cell membrane; orange line, nuclear membrane. Data are shown as mean ± s.e.m. Statistically significant differences were determined by paired two-sided t -tests (for total inclusions, total inclusion with content, inclusion with axon terminal, empty inclusion, endoplasmic reticulum, contact with neuron and contact with axon terminal) or two-sided Wilcoxon matched-pairs signed-rank test (for contact with cleft); * $P \leq 0.05$.

Arg1 microglial deletion impacts cholinergic innervation
The forebrain cholinergic system has been involved in the maintenance of hippocampal neurons and in learning, memory and other

behavioral processes³⁹. Cholinergic inputs to the hippocampus arise from the medial septal (MS) nucleus and the nucleus of the diagonal band of Broca (DB⁴⁰; areas adjacent to ARG1⁺ microglia localization),

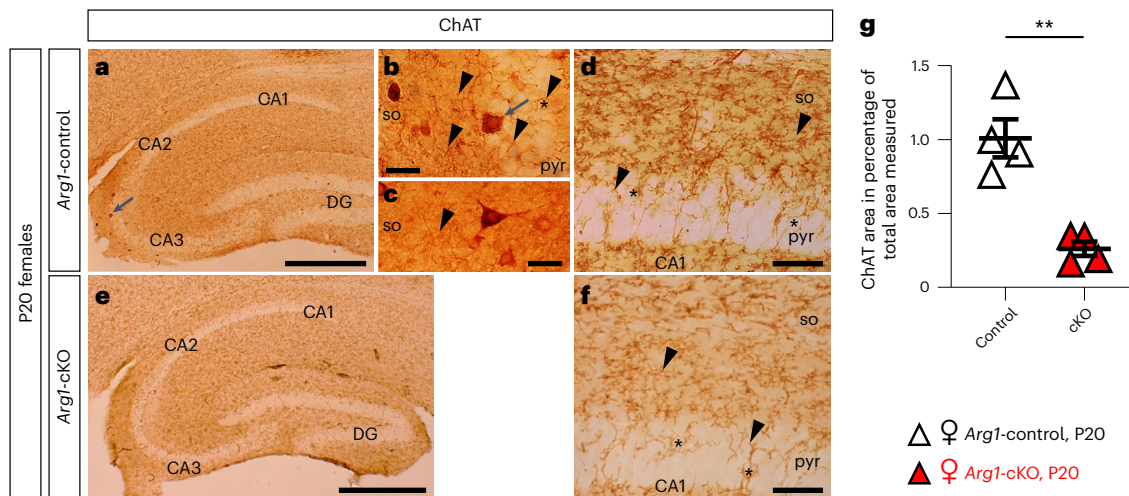


Fig. 6 | The *Arg1*-cKO hippocampi of 2- to 3-month-old female mice receive reduced cholinergic innervation. a–f, Microphotographs of sagittal sections of *Arg1*-control (a–d) and *Arg1*-cKO (e,f) P20 female hippocampi. ChAT immunoreactivity was revealed by using DAB as a chromogen. Triangular or ovoid immunoreactive ChAT interneurons were observed in the CA3 field of the *Arg1*-control hippocampus (a,b, arrows). Cholinergic axons show the characteristic varicosities (b–d,f, arrowheads) of the boutons of en passant

synapses. At the pyramidal cell layer (pyr), immunoreactive fibers delineate the pyramidal neuronal somata (so; d,f, asterisk). **g**, Quantitative analysis demonstrates that the female *Arg1*-cKO hippocampus receives less cholinergic innervation than the *Arg1*-control hippocampus; $P = 0.0016$. Each triangle corresponds to one animal ($n = 4$). Scale bars, 500 μm (a,e), 50 μm (d,f) and 20 μm (b,c). Data are shown as mean \pm s.e.m. Statistically significant differences were determined by an unpaired two-sided *t*-test; ** $P \leq 0.01$.

was found in *Arg1*-cKO female mice. Male *Arg1*-cKO mice also exhibited reduced, but not impaired, E-LTP and L-LTP (Fig. 8b,c).

To analyze the short-term potentiation for the different mice used, the means of the first sweeps after applying the plasticity protocol in each experiment were analyzed. Our data indicate that short-term potentiation in the Schaffer collateral–CA1 pathway is not affected in any of the groups studied (Fig. 8d).

To determine the site of expression of LTP, we analyzed paired-pulse facilitation ratios (PPRs) at baseline and 120 min after the application of the induction protocol. The analysis of PPRs before and after LTP did not show differences between animal groups, suggesting that this form of LTP is postsynaptically expressed (Fig. 8e). Finally, to investigate if the basal synaptic transmission is altered, a stimulus–response curve (0.1–0.6 mA; mean of five field excitatory postsynaptic potentials (fEPSPs) at each stimulation strength) was compiled. No differences between groups were found. These data indicate that the differences observed in LTP magnitude between all the groups of mice are not due to a defect in basal synaptic transmission (Fig. 8f).

Discussion

Compiling data show that microglia are not a homogenous population that respond stereotypically to extrinsic stimuli but instead are a heterogeneous cell type that exhibit distinct transcriptomic profiles^{14–18} and ultrastructural⁴⁶ differences, a diversity that is especially pronounced during early postnatal development (reviewed in ref. 8). Here, we report a microglial subtype morphologically indistinguishable from neighboring microglia, which exhibits a substantially different transcriptome, dynamic spatiotemporal localization and functional specialization. We show that the enzyme ARG1 is highly expressed in this microglial subtype and is essential for proper brain development. We provide compelling evidence for a critical role of ARG1⁺ microglia in shaping neuronal circuits involved in cognition. Supporting this, microglial *Arg1* knockout results in impaired neuronal plasticity and cognitive deficits in mice. Previous studies have shown that whole-body *Arg1* knockout in mice is postnatally lethal and causes neurotoxicity³⁵. In humans, ARG1 deficiency is a rare autosomal disease^{35,36}. As in mice, ARG1-deficient individuals show neurological problems evidenced by progressive neurological and cognitive impairment leading to various

degrees of intellectual disability³⁵. Most interestingly, the vast majority of individuals whose peripheral symptoms can be managed through diet or drug therapy still continue to suffer from cognitive deficits³⁵. Whether human pathology is linked specifically to ARG1 deficiency in microglia requires further investigation.

Our RNA-seq analysis showed robust expression of typical homeostatic genes, including, among others, *Csf1r*, *Cst3*, *Cx3cr1*, *Hexb*, *P2ry12*, *Sparc*, *Tmem119* and *Siglech*^{14,31–33,47,48}, indicating that our cell sorting strategy was highly specific for isolating microglia. Recent extensive transcriptomic analyses of microglia have identified several microglia subsets during early postnatal development^{14,16,17,22}. One microglia subset was originally identified by high expression of CD11c and insulin-like growth factor 1 and was associated with the corpus callosum and cerebellar white matter²². Subsequent studies using transcriptomic analysis of microglia at the single-cell level confirmed the existence of this microglia subtype, which was further defined as tract-associated microglia¹⁷ or proliferative region-associated microglia¹⁶. Intriguingly, this microglial subtype was characterized by downregulation of homeostatic microglia markers along with upregulation of several genes typically found under disease conditions (disease-associated microglia)^{16,17,32,33}, thus sharing some molecular features with the ARG1⁺ microglia subtype. However, tract-associated microglia do not upregulate the expression of *Arg1* (refs. 16,17), which, together with the high enrichment of this microglia subtype in axon tracts and their amoeboid morphology, fully contrast with the phenotype observed in the ARG1⁺ microglial subtype^{16,17}. We may wonder how this microglial subtype has escaped identification from most transcriptomic studies performed during postnatal development. One possible explanation is that ARG1⁺ microglia present both spatial and temporal aspects, and their numbers remained limited compared to the overall microglial cell population. Stevens and colleagues¹⁷ recently identified a small microglia cluster (cluster 1 (the smallest identified cluster in their study) comprising about 0.5% of total microglia), which displays strong upregulation of *Arg1*. The experimental design of the two studies present differences, including the age of animals used (P4/P5 versus P13), genetic background (C57BL/6J versus 129S4/SvJae), area where cells were isolated (no specific location versus the BF), cell isolation protocol and sequencing technology.

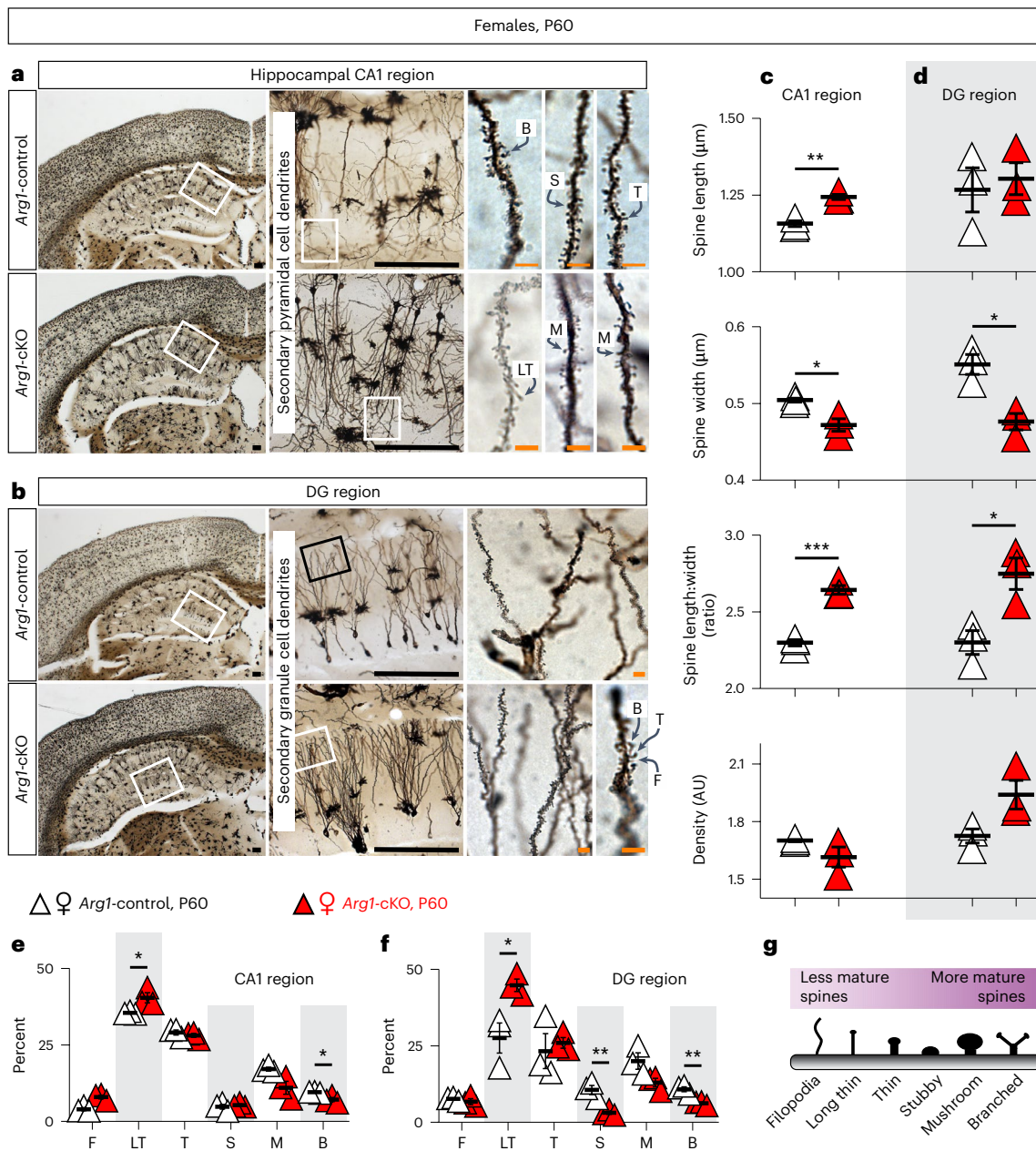


Fig. 7 | *Arg1* microglial cKO affects dendrite maturation in the hippocampus of 2- to 3-month-old female mice. **a, b.** Coronal Golgi–Cox-stained sections of female P60 *Arg1*-cKO and control brains. Hippocampal CA1 and DG regions in which secondary pyramidal and secondary granule cell dendrites arise from the main one, respectively, were used for spine counts. **c–f.** Graphical representation of differences between spines in the hippocampal CA1 (**c, e**) and DG (**d, f**). CA1 length, $P = 0.0023$; CA1 width, $P = 0.0191$; CA1 length:width, $P = 0.0006$; DG width, $P = 0.0114$; DG length:width, $P = 0.0251$; CA1 long thin (%), $P = 0.0571$; CA1 branched (%), $P = 0.0273$; DG long thin (%), $P = 0.0318$; DG stubby (%), $P = 0.0087$;

DG branched (%), $P = 0.0066$; AU, arbitrary units. **g.** The six main spine categories according to their morphological characteristics, including filopodia (F), long thin (LT), thin (T), stubby (S), mushroom (M) and branched (B). Each triangle corresponds to one animal (female *Arg1*-control $n = 3$; female *Arg1*-cKO $n = 3$; male *Arg1*-control $n = 2$; male *Arg1*-cKO $n = 3$). Black scale bars, 200 μm . Orange scale bars, 5 μm . Data are shown as mean \pm s.e.m. Statistically significant differences were determined by unpaired two-sided t -tests or two-sided Mann–Whitney U -test (for filopodia); * $P \leq 0.05$, ** $P \leq 0.01$ and *** $P = 0.0006$.

Yet, the two cell populations display a strong upregulation of genes such as *Apoe*, *C3*, *Lgals3*, *Mgl2* and *Igf1* (Extended Data Fig. 7g) and are more prominent during early postnatal stages¹⁷, thus validating the ARG1⁺ microglial subtype independently. In addition, the cluster 1 size shows sex-specific variation, with enrichment in female mice¹⁷. This observation is important as it provides strong support to the expanding literature about sex differences in microglia^{23,24} and it suggests directions for future research to understand differences in the behavioral studies we observed in this study. Although here

we report ARG1⁺ microglia in both sexes that exist in equal numbers (Extended Data Fig. 6) and have the same transcriptomic profiles (Extended Data Fig. 5b), this contradiction only highlights that a systematic analysis of microglial phenotypes needs to be performed to understand how microglial subtypes contribute to physiology and disease of the brain^{8,9}. Taken together, we can conclude that ARG1⁺ microglia are a developmentally regulated subtype that display a distinctive molecular signature and have a specific function in shaping the brain.

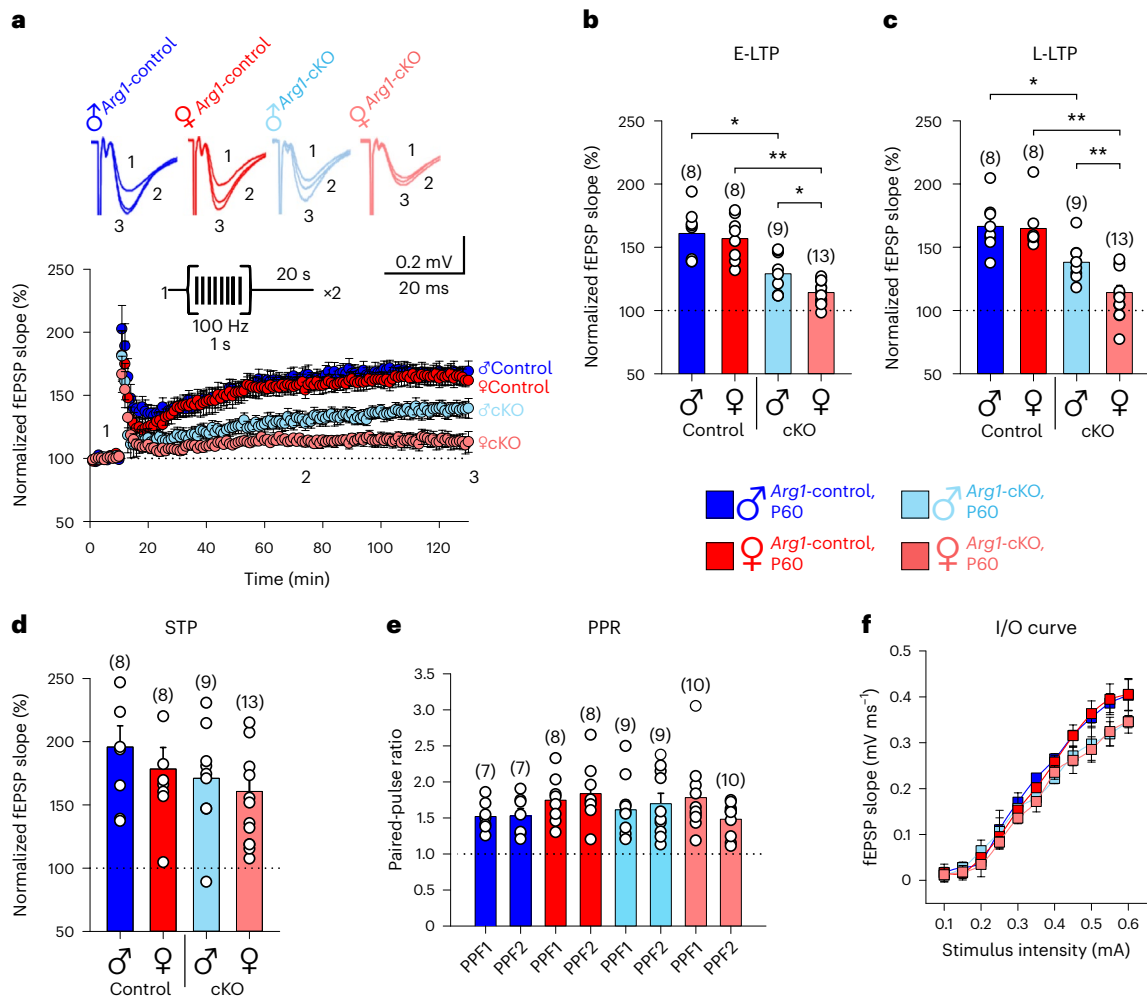


Fig. 8 | LTP is prevented in 2- to 3-month-old female *Arg1*-cKO mice. **a**, Time course of fEPSPs before and after LTP induction in male *Arg1*-control (blue circles; $n = 8$), female *Arg1*-control (red circles; $n = 8$), male *Arg1*-cKO (light blue circles; $n = 9$) and female *Arg1*-cKO (light red circles; $n = 13$) mice. The inset traces show fEPSPs before (1) and 60 min (2) and 120 min (3) after the plasticity protocol. *Arg1*-control male: $161 \pm 7\%$ (E-LTP) and $167 \pm 7\%$ (L-LTP); *Arg1*-control female: $157 \pm 6\%$ (E-LTP) and $165 \pm 6\%$ (L-LTP); *Arg1*-cKO male: $129 \pm 6\%$ (E-LTP) and $139 \pm 6\%$ (L-LTP); *Arg1*-cKO female: $114 \pm 3\%$ (E-LTP) and $112 \pm 4\%$ (L-LTP). **b, c**, Histograms show a summary of the results for E-LTP (**b**) and L-LTP (**c**). E-LTP, *Arg1*-control male versus *Arg1*-cKO male, $P = 0.003$; E-LTP, *Arg1*-control female versus *Arg1*-cKO female, $P < 0.001$; E-LTP, *Arg1*-cKO male versus *Arg1*-cKO female, $P = 0.015$; L-LTP, *Arg1*-control male versus *Arg1*-cKO male, $P = 0.006$; L-LTP, *Arg1*-control female versus *Arg1*-cKO female, $P < 0.001$; L-LTP, *Arg1*-cKO male versus *Arg1*-cKO female,

$P < 0.001$. **d**, Short-term synaptic potentiation (STP) is not affected in any of the groups studied. *Arg1*-control male: $196 \pm 17\%$, $n = 8$; *Arg1*-control female: $178 \pm 17\%$, $n = 8$; *Arg1*-cKO male: $171 \pm 16\%$, $n = 9$; *Arg1*-cKO female: $161 \pm 14\%$, $n = 13$. **e**, PPR summary data. *Arg1*-control male: 1.53 ± 0.1 after LTP versus 1.52 ± 0.08 at baseline, $n = 7$; *Arg1*-control female: 1.84 ± 0.15 after LTP versus 1.75 ± 0.12 at baseline, $n = 8$; *Arg1*-cKO male: 1.69 ± 0.14 after LTP versus 1.61 ± 0.13 at baseline, $n = 9$; *Arg1*-cKO female: 1.49 ± 0.08 after LTP versus 1.78 ± 0.16 at baseline, $n = 10$; PPF, paired-pulse facilitation. **f**, Input-output (I/O) curves for *Arg1*-control male ($n = 6$), *Arg1*-control female ($n = 6$), *Arg1*-cKO male ($n = 6$) and *Arg1*-cKO female ($n = 6$) mice. The number of slices is shown in parentheses. Data are shown as mean \pm s.e.m. Statistically significant differences were determined by unpaired two-sided *t*-tests, with *P* values corrected using the Bonferroni method for multiple comparisons; * $P < 0.05$ and ** $P < 0.01$.

An outstanding observation of the present study was the highly enriched presence of ARG1⁺ microglia within the BF of the developing brain, where main cholinergic groups are located and known to play major roles in cognitive processes, such as attention, learning and memory^{49,50}. Remarkably, we found substantial impairment in long-term memory in females but not in males lacking *Arg1* in microglia, thus sustaining a sexual dimorphism related to the ARG1⁺ microglia subtype. Importantly, motor behavior was not affected in *Arg1*-cKO mice, therefore raising the possibility that forebrain cholinergic dysfunction underlies the cognitive deficits in female mice lacking *Arg1*. Notably, the appearance of ARG1⁺ microglia mimicked the temporal maturation of main cholinergic markers, including ChAT and acetylcholinesterase expressions and activities, which rise progressively until reaching adult levels between the third and fourth postnatal week^{50,51}. Additionally, dendritic growth and branching, along with the increase in perikaryal

size, starts within the first 3 postnatal weeks to reach adult levels by P30 (ref. 51), again fully coincident with the appearance of ARG1⁺ microglia in the BF. Our immunohistochemical and ultrastructural analysis demonstrated the interaction between cholinergic neurons/processes and ARG1⁺ microglia, and, hence, the possibility that this microglial subtype contributes to the maturation of the BF cholinergic system is certainly plausible. Supporting this, a deficient cholinergic innervation to the hippocampus was evident in *Arg1*-cKO female mice, a critical process given the vital role of cholinergic innervation in the regulation of synaptic communication and plasticity within the hippocampus⁵². During development, spines mature from a thin, elongated shape to a mushroom-like structure⁵³, a process critically involved in LTP⁵⁴. We provide compelling evidence that both forms of synaptic plasticity are largely affected in the hippocampi of *Arg1*-cKO female mice, thus raising the importance of this microglia subtype in regulating critical

aspects of hippocampus-dependent long-term memory. First, our morphological analysis revealed that pyramidal and dentate spines showed an increased proportion of immature spines and a decreased proportion of mature spines in females. It is important to highlight that dendritic spines represent the main unitary postsynaptic compartment for excitatory input, the basis for LTP induction⁵³. Among the different forms of synaptic plasticity, that relying on NMDA receptor-dependent LTP in the CA1 region of the hippocampus is probably the most studied given its close correlation with learning and memory⁵³. In turn, LTP and behavioral paradigms, such as spatial learning memory, are tightly associated processes⁵⁵. Given the striking sexual dimorphism observed for the ARG1⁺ microglial subtype, we wanted to know how male and female *Arg1*-cKO mice induced and expressed LTP at Schaffer collateral–CA1 synapses. The electrophysiological analysis revealed that *Arg1* is required for long-term plasticity in both male and female mice, therefore substantiating our RNA-seq transcriptional analysis showing similar molecular signatures from ARG1⁺ microglia in both sexes. However, a substantial functionally relevant difference was observed in terms of requirement between males and females. While LTP was present but reduced in magnitude in *Arg1*-cKO males, the induction of LTP in *Arg1*-cKO females was impaired. These results indicate a different requirement of microglial *Arg1* for males and females, being critical for females. By analyzing PPR, we confirmed the postsynaptic locus of this form of LTP as previously established⁵⁶. Interestingly, and consistent with this, short-term plasticity was not altered in any genotype. By studying the characteristics of input–output curves, no differences were found between different genotypes. These results indicate that the differences found in LTP are not due to changes in the presynaptic machinery of release. In fact, changes were found postsynaptically in the distribution-type of dendritic spines between male and female mice. However, we cannot exclude the possibility that phenotypes observed in the hippocampus are due to a direct impact from local microglia (for example, through low but biologically important *Arg1* mRNA expression by these cells), we did not observe ARG1⁺ microglia in this area. In conclusion, electrophysiological results fully agree with the changes observed in (1) dendritic spine maturation in the hippocampus and (2) behavioral results demonstrating that a disruption of LTP in *Arg1*-cKO females coincides with defects in long-term memory in the same mice.

Previous reports have identified intrinsic roles of early postnatal microglia in synaptic stripping and pruning, modulation of synaptic transmission and synaptogenesis, apoptotic cell corpse removal and neuron survival⁷⁸. In this study, we have identified ARG1⁺ microglia, morphologically indistinguishable from ARG1⁺ microglia, which emerge as a highly dynamic subtype involved in elaboration and maturation of the BF cholinergic system and hippocampal synaptic plasticity in female mice. Maturation of this system is of critical importance in developmental disorders, including autism⁵⁰, and Alzheimer's disease⁵⁷. Of note, the involvement of microglia in Alzheimer's disease pathology is highly recognized in the field⁵⁸, and two-thirds of individuals suffering from Alzheimer's disease are women, whose underlying mechanism is not explained by only differences in longevity⁵⁹. Our study provides a step toward understanding how ARG1⁺ microglia regulate the development of the BF and highlights the potential involvement in pathological conditions.

Online content

Any methods, additional references, Nature Portfolio reporting summaries, source data, extended data, supplementary information, acknowledgements, peer review information; details of author contributions and competing interests; and statements of data and code availability are available at <https://doi.org/10.1038/s41593-023-01326-3>.

References

1. Tau, G. Z. & Peterson, B. S. Normal development of brain circuits. *Neuropsychopharmacology* **35**, 147–168 (2010).
2. Monier, A. et al. Entry and distribution of microglial cells in human embryonic and fetal cerebral cortex. *J. Neuropathol. Exp. Neurol.* **66**, 372–382 (2007).
3. Ginhoux, F. et al. Fate mapping analysis reveals that adult microglia derive from primitive macrophages. *Science* **330**, 841–845 (2010).
4. De, S. et al. Two distinct ontogenies confer heterogeneity to mouse brain microglia. *Development* **145**, dev152306 (2018).
5. Squarzone, P. et al. Microglia modulate wiring of the embryonic forebrain. *Cell Rep.* **8**, 1271–1279 (2014).
6. Thion, M. S., Ginhoux, F. & Garel, S. Microglia and early brain development: an intimate journey. *Science* **362**, 185–189 (2018).
7. Zengeler, K. E. & Lukens, J. R. Innate immunity at the crossroads of healthy brain maturation and neurodevelopmental disorders. *Nat. Rev. Immunol.* **21**, 454–468 (2021).
8. Stratoulia, V., Venero, J. L., Tremblay, M. & Joseph, B. Microglial subtypes: diversity within the microglial community. *EMBO J.* **38**, e101997 (2019).
9. Keane, L., Cheray, M., Blomgren, K. & Joseph, B. Multifaceted microglia—key players in primary brain tumour heterogeneity. *Nat. Rev. Neurol.* **17**, 243–259 (2021).
10. Hambardzumyan, D., Gutmann, D. H. & Kettenmann, H. The role of microglia and macrophages in glioma maintenance and progression. *Nat. Neurosci.* **19**, 20–27 (2016).
11. Hickman, S., Izzy, S., Sen, P., Morsett, L. & El Khoury, J. Microglia in neurodegeneration. *Nat. Neurosci.* **21**, 1359–1369 (2018).
12. Shen, X. et al. Glioma-induced inhibition of caspase-3 in microglia promotes a tumor-supportive phenotype. *Nat. Immunol.* **17**, 1282–1290 (2016).
13. Burguillos, M. A. et al. Caspase signalling controls microglia activation and neurotoxicity. *Nature* **472**, 319–324 (2011).
14. Masuda, T. et al. Spatial and temporal heterogeneity of mouse and human microglia at single-cell resolution. *Nature* **566**, 388–392 (2019).
15. Van Hove, H. et al. A single-cell atlas of mouse brain macrophages reveals unique transcriptional identities shaped by ontogeny and tissue environment. *Nat. Neurosci.* **22**, 1021–1035 (2019).
16. Li, Q. et al. Developmental heterogeneity of microglia and brain myeloid cells revealed by deep single-cell RNA sequencing. *Neuron* **101**, 207–223 (2019).
17. Hammond, T. R. et al. Single-cell RNA sequencing of microglia throughout the mouse lifespan and in the injured brain reveals complex cell-state changes. *Immunity* **50**, 253–271 (2019).
18. Jordão, M. J. C. et al. Single-cell profiling identifies myeloid cell subsets with distinct fates during neuroinflammation. *Science* **363**, eaat7554 (2019).
19. Osman, A. M. et al. Radiation triggers a dynamic sequence of transient microglial alterations in juvenile brain. *Cell Rep.* **31**, 107699 (2020).
20. Schafer, D. P. et al. Microglia sculpt postnatal neural circuits in an activity and complement-dependent manner. *Neuron* **74**, 691–705 (2012).
21. Parkhurst, C. N. et al. Microglia promote learning-dependent synapse formation through brain-derived neurotrophic factor. *Cell* **155**, 1596–1609 (2013).
22. Wlodarczyk, A. et al. A novel microglial subset plays a key role in myelinogenesis in developing brain. *EMBO J.* **36**, 3292–3308 (2017).
23. Lenz, K. M., Nugent, B. M., Haliyur, R. & McCarthy, M. M. Microglia are essential to masculinization of brain and behavior. *J. Neurosci.* **33**, 2761–2772 (2013).
24. Sorge, R. E. et al. Different immune cells mediate mechanical pain hypersensitivity in male and female mice. *Nat. Neurosci.* **18**, 1081–1083 (2015).

25. Reese, T. A. et al. Chitin induces accumulation in tissue of innate immune cells associated with allergy. *Nature* **447**, 92–96 (2007).
26. Renier, N., et al. Mapping of brain activity by automated volume analysis of immediate early genes. *Cell* **165**, 1789–1802 (2016).
27. Ballinger, E. C., Ananth, M., Talmage, D. A. & Role, L. W. Basal forebrain cholinergic circuits and signaling in cognition and cognitive decline. *Neuron* **91**, 1199–1218 (2016).
28. Semba, K. Phylogenetic and ontogenetic aspects of the basal forebrain cholinergic neurons and their innervation of the cerebral cortex. *Prog. Brain Res.* **145**, 3–43 (2004).
29. Goldmann, T. et al. Origin, fate and dynamics of macrophages at central nervous system interfaces. *Nat. Immunol.* **17**, 797–805 (2016).
30. Butovsky, O. & Weiner, H. L. Microglial signatures and their role in health and disease. *Nat. Rev. Neurosci.* **19**, 622–635 (2018).
31. Bennett, M. L. et al. New tools for studying microglia in the mouse and human CNS. *Proc. Natl Acad. Sci. USA* **113**, E1738–E1746 (2016).
32. Krasemann, S. et al. The TREM2–APOE pathway drives the transcriptional phenotype of dysfunctional microglia in neurodegenerative diseases. *Immunity* **47**, 566–581 (2017).
33. Keren-Shaul, H. et al. A unique microglia type associated with restricting development of Alzheimer’s disease. *Cell* **169**, 1276–1290 (2017).
34. Tremblay, M., Lowery, R. L. & Majewska, A. K. Microglial interactions with synapses are modulated by visual experience. *PLoS Biol.* **8**, e1000527 (2010).
35. Sin, Y. Y., Baron, G., Schulze, A. & Funk, C. D. Arginase-1 deficiency. *J. Mol. Med.* **93**, 1287–1296 (2015).
36. Jain-Ghai, S., Nagamani, S. C., Blaser, S., Siriwardena, K. & Feigenbaum, A. Arginase I deficiency: severe infantile presentation with hyperammonemia: more common than reported? *Mol. Genet Metab.* **104**, 107–111 (2011).
37. Dean, D. M. & Sanders, M. M. Ten years after: reclassification of steroid-responsive genes. *Mol. Endocrinol.* **10**, 1489–1495 (1996).
38. Cloots, R. H. E. et al. Arginase 1 deletion in myeloid cells affects the inflammatory response in allergic asthma, but not lung mechanics, in female mice. *BMC Pulm. Med.* **17**, 158 (2017).
39. Mohapel, P., Leanza, G., Kokaia, M. & Lindvall, O. Forebrain acetylcholine regulates adult hippocampal neurogenesis and learning. *Neurobiol. Aging* **26**, 939–946 (2005).
40. Amaral, D. & Lavenex, P. in *The Hippocampus Book* (eds Anderson, P. et al.) Ch. 3 (Oxford Univ. Press, 2007).
41. Aznavour, N., Mechawar, N. & Descarries, L. Comparative analysis of cholinergic innervation in the dorsal hippocampus of adult mouse and rat: a quantitative immunocytochemical study. *Hippocampus* **12**, 206–217 (2002).
42. Ramón, S. & Cajal, Y. *Textura del Sistema Nervioso del Hombre y de los Vertebrados* (Imprenta y Librería de Nicolás Moya, Madrid (1899–1904), 1904).
43. Berry, K. P. & Nedivi, E. Spine dynamics: are they all the same? *Neuron* **96**, 43–55 (2017).
44. Pérez-Villegas, E. M. et al. Mutation of the HERC1 ubiquitin ligase impairs associative learning in the lateral amygdala. *Mol. Neurobiol.* **55**, 1157–1168 (2018).
45. Alvarez, V. A. & Sabatini, B. L. Anatomical and physiological plasticity of dendritic spines. *Annu. Rev. Neurosci.* **30**, 79–97 (2007).
46. Bisht, K. et al. Dark microglia: a new phenotype predominantly associated with pathological states. *Glia* **64**, 826–839 (2016).
47. Butovsky, O. et al. Identification of a unique TGF- β -dependent molecular and functional signature in microglia. *Nat. Neurosci.* **17**, 131–143 (2014).
48. Hickman, S. E. et al. The microglial sensome revealed by direct RNA sequencing. *Nat. Neurosci.* **16**, 1896–1905 (2013).
49. Lin, S. C., Brown, R. E., Hussain Shuler, M. G., Petersen, C. C. & Kepecs, A. Optogenetic dissection of the basal forebrain neuromodulatory control of cortical activation, plasticity, and cognition. *J. Neurosci.* **35**, 13896–13903 (2015).
50. Allaway, K. C. & Machold, R. Developmental specification of forebrain cholinergic neurons. *Dev. Biol.* **421**, 1–7 (2017).
51. Thal, L. J., Gilbertson, E., Armstrong, D. M. & Gage, F. H. Development of the basal forebrain cholinergic system: phenotype expression prior to target innervation. *Neurobiol. Aging* **13**, 67–72 (1992).
52. Drever, B. D., Riedel, G. & Platt, B. The cholinergic system and hippocampal plasticity. *Behav. Brain Res* **221**, 505–514 (2011).
53. Hering, H. & Sheng, M. Dendritic spines: structure, dynamics and regulation. *Nat. Rev. Neurosci.* **2**, 880–888 (2001).
54. Engert, F. & Bonhoeffer, T. Dendritic spine changes associated with hippocampal long-term synaptic plasticity. *Nature* **399**, 66–70 (1999).
55. Whitlock, J. R., Heynen, A. J., Shuler, M. G. & Bear, M. F. Learning induces long-term potentiation in the hippocampus. *Science* **313**, 1093–1097 (2006).
56. Malenka, R. C. & Nicoll, R. A. Long-term potentiation—a decade of progress? *Science* **285**, 1870–1874 (1999).
57. Hampel, H. et al. The cholinergic system in the pathophysiology and treatment of Alzheimer’s disease. *Brain* **141**, 1917–1933 (2018).
58. Heneka, M. T. et al. Neuroinflammation in Alzheimer’s disease. *Lancet Neurol.* **14**, 388–405 (2015).
59. Zhu, D., Montagne, A. & Zhao, Z. Alzheimer’s pathogenic mechanisms and underlying sex difference. *Cell. Mol. Life Sci.* **78**, 4907–4920 (2021).

Publisher’s note Springer Nature remains neutral with regard to jurisdictional claims in published maps and institutional affiliations.

Open Access This article is licensed under a Creative Commons Attribution 4.0 International License, which permits use, sharing, adaptation, distribution and reproduction in any medium or format, as long as you give appropriate credit to the original author(s) and the source, provide a link to the Creative Commons license, and indicate if changes were made. The images or other third party material in this article are included in the article’s Creative Commons license, unless indicated otherwise in a credit line to the material. If material is not included in the article’s Creative Commons license and your intended use is not permitted by statutory regulation or exceeds the permitted use, you will need to obtain permission directly from the copyright holder. To view a copy of this license, visit <http://creativecommons.org/licenses/by/4.0/>.

© The Author(s) 2023

¹Institute of Environmental Medicine, Toxicology Unit, Karolinska Institutet, Stockholm, Sweden. ²Neuroscience Center, HiLIFE, University of Helsinki, Helsinki, Finland. ³Instituto de Biomedicina de Sevilla, IBIS/Hospital Universitario Virgen del Rocío/CSIC, Universidad de Sevilla, Seville, Spain.

⁴Department of Medical Biochemistry and Biophysics, Karolinska Institutet, Stockholm, Sweden. ⁵Department of Women’s and Children’s Health, Karolinska Institutet, Stockholm, Sweden. ⁶Department of Physiology, Anatomy and Cellular Biology, University of Pablo de Olavide, Seville, Spain.

⁷Department of Molecular Medicine, Université Laval, and Axe Neurosciences, Centre de Recherche du CHU de Québec-Université Laval, Laval, Quebec, Canada. ⁸Division of Medical Sciences, University of Victoria, Victoria, British Columbia, Canada. ⁹Department of Neurodegenerative Diseases and Gerontopsychiatry, University of Bonn, Bonn, Germany. ¹⁰Bioinformatics and Expression Analysis Core Facility, Department of Biosciences and Nutrition,

Karolinska Institutet, Stockholm, Sweden. ¹¹Department of Molecular Biology and Umeå Centre for Microbial Research (UCMR), Umeå University, Umeå, Sweden. ¹²Clinical Epidemiology and Biostatistics, School of Medical Sciences, Örebro University, Örebro, Sweden. ¹³Unit of Integrative Epidemiology, Institute of Environmental Medicine, Karolinska Institutet, Stockholm, Sweden. ¹⁴Faculty of Pharmacy, Drug Research Program, University of Helsinki, Helsinki, Finland. ¹⁵Luxembourg Centre for Systems Biomedicine, University of Luxembourg, Belvaux, Luxembourg. ¹⁶Department of Infectious Diseases and Immunology, University of Massachusetts Medical School, Worcester, MA, USA. ¹⁷Department of Paediatric Oncology, Karolinska University Hospital, Stockholm, Sweden. ¹⁸These authors contributed equally: Shigeaki Kanatani, Ahmed M. Osman, Lily Keane. ¹⁹These authors jointly supervised this work: Jose L. Venero, Bertrand Joseph. ✉ e-mail: vassilis.stratoulas@ki.se; bertrand.joseph@ki.se

Methods

Animals

All experimental animal protocols in the present study were in accordance with the respective national, federal and institutional regulations, that is, the Guidelines of the European Union Council, following Swedish regulations for the use of laboratory animals and approved by the Regional Animal Research Ethical Board, Stockholm, Sweden (ethical permits N248/13), and the Scientific Committee of Instituto de Investigación y Formación Agraria y Pesquera, Consejería de Agricultura, Pesca, Agua y Desarrollo Rural of Junta de Andalucía (Spain; 03/05/2018/069) and in conformity with the Canada Council on Animal Care guidelines. C57BL/6J (WT; Charles River), YARG (The Jackson Laboratory, stock 015857), *Cx3cr1^{GFP}* (The Jackson Laboratory, stock 005582), *Arg1^{fl/fl}* (The Jackson Laboratory, stock 008817) and *Cx3cr1^{CreER}* (The Jackson Laboratory, stock 021160) mice were used and maintained under a 12-h light/12-h dark cycle at 22–25 °C with access to food and water ad libitum.

Generation of microglia-specific ARG1-deficient mice (*Arg1-cKO*).

Arg1^{fl/fl} mice with the *Arg1* allele bearing *loxP* sites flanking exons 7 and 8 were crossed with *Cx3cr1^{CreER}* mice to generate *Arg1^{fl/fl}Cx3cr1^{CreER/+}* (*Arg1-cKO*) and *Arg1^{fl/fl}Cx3cr1^{CreER/-}* (*Arg1-control*) mice (Fig. 5a). The deletion was induced after daily tamoxifen treatment for 2 or 3 consecutive days starting at P1 (Fig. 5b). All mice (*Cre⁺* and *Cre⁻*) were injected with tamoxifen at a dose of 250 µg per pup. Genotyping of the mice was done by PCR analyses of finger DNA using primers as presented in Supplementary Table 2.

Tissue preparation, immunohistochemistry and confocal laser microscopy

Animals were deeply anesthetized with sodium pentobarbital, transcardially perfused with 0.9% sodium chloride and fixed with 4% paraformaldehyde in 0.1 M phosphate buffer (pH 7.4). Brains were collected and postfixed in the same fixative for 24 h and transferred to 30% sucrose in 0.1 M phosphate buffer for cryoprotection for a minimum of 3 d. Brains were cryosectioned using a sliding microtome (Leica, SM2000R) into 25-µm free-floating sections and stored as 1:12 series at 4 °C. When necessary, antigen retrieval was performed by heat-induced antigen retrieval, followed by PBS washes, permeabilization with 0.3% Triton X-100 in PBS and blocking with 0.3% Triton X-100 and 10% donkey serum in PBS. Sections were washed in PBS before incubation with secondary antibodies (Alexa Fluor). Sections were washed in PBS, counterstained with Hoechst or DAPI, further washed in PBS and mounted in Fluoromount-G.

For DAB staining, brain sections were deparaffinized and hydrated through treatment with xylenes and a graded alcohol series, followed by treatment with 0.6% hydrogen peroxide in TBS. Sections were washed in TBS, permeabilized in TBS Tween 20 (0.1%), blocked with TBS Tween 20 (0.1%) and 5% normal serum and incubated with primary antibody in blocking solution overnight at 4 °C. Sections were washed with TBS and incubated with SignalStain Boost detection reagent and SignalStain DAB. For information about antibodies, reagents and hardware and software used, see Supplementary Table 2.

Manual cell number quantification. Microglia and ChAT⁺ somas were identified based on corresponding markers. The numbers of animals used are denoted by circles, squares and/or triangles.

Intensity analyses. The mean intensity of the fluorescent marker CD68 was measured by performing mask outlining of the ARG1 area using the same value of threshold in each image, followed by automatic measurement of the mean intensity inside these areas using Fiji ImageJ software⁶⁰. The percentage of ChAT labeling in the female CA1 was determined automatically by defining outline masks based on brightness thresholds with Fiji software.

Morphometric analysis. Individual microglia from the BF/vStr, with their nuclei in the center of the z plane, were selected. Three-dimensional confocal z stacks were automatically reconstructed using a self-customized Python-based script⁶¹. Reconstructions were visually checked using the ImageJ plugin ‘simple neurite tracer’. Each cell was individually extracted, and the number of branches, path length, branch order and process volume were quantified using the open-source software L-measure. Four mice per developmental stage were examined. At least 15 (P10) and 32 (P28) microglia of each phenotype were analyzed. For information about antibodies and hardware and software used, see Supplementary Table 2.

Golgi–Cox staining. Segments of secondary dendrites of pyramidal neurons located at the level of the stratum radiatum (CA1) and granule cell dendritic spines of the outer third of the suprapyramidal blade (DG) were considered for quantitative analysis. Dendrite segments from 15 to 20 µm in length filled by the mercuric reaction of the Golgi–Cox method were used.

iDISCO+

iDISCO+ immunostaining and tissue clearing. iDISCO+ immunostaining and tissue clearing was performed as previously published^{26,62}. P10 and P28 WT male mouse brains were perfused using 4% paraformaldehyde and fixed overnight at 4 °C. Brains were washed with PBS, cut into half hemispheres, treated with an up-series of methanol solutions and stored at –20 °C. Samples were treated with 5% hydroxyperoxide in methanol overnight at 4 °C, treated with a reverse concentration of methanol solution and washed with iDISCO washing buffer. After permeabilization and blocking, samples were incubated with primary antibodies for 5–7 d at 37 °C with gentle rotation. Samples were then washed with iDISCO washing buffer for 1 d and incubated with secondary antibodies for 5–7 d at 37 °C. Samples were washed with iDISCO wash buffer (1 d) with gentle rotation at 37 °C. The immunostained hemispheres were treated with an up-series of methanol solution. Samples were incubated in 33% methanol and 66% dichloromethane for 3 h and 100% dichloromethane for 15 min twice and were transferred in dibenzyl ether (DBE). After 1 d of incubation with DBE, the DBE solution was changed to fresh solution and incubated for 1 d before imaging. For information about antibodies and reagents used, see Supplementary Table 2.

iDISCO+ imaging acquisition. Cleared brain images were acquired with a COLM microscope⁶³. The hemisphere was placed in a quartz cuvette filled with DBE, and the position was fixed using silicone blocks. Immunostaining signal was acquired with a 647- or 561-nm channel, and autofluorescence was assessed with a 488- or 405-nm laser channel for image registration. The original image resolution was 0.585, 0.585 and 5 µm in the x, y and z axes. For information about materials used, see Supplementary Table 2.

iDISCO+ image analysis. Original TIFF files (16 bit) were downsampled to an isotropic resolution of 5 µm and converted into 8 bit by custom MATLAB script and Fiji⁶⁴. Each z-stack image was stitched by TeraStitcher⁶⁵. The stitched images were processed by a series of processing filters (unsharp mask, background subtraction, integral filter and fast Fourier transform filter) in ImageJ and Amira 3D software (Thermo Fisher Scientific). ARG1⁺ and IBA1⁺ cells were recognized by signal intensity and morphology. After removing blood vessels manually in Amira segmentation editor, ARG1⁺ and IBA1⁺ cells were segmented by global threshold segmentation. Segmented images were labeled, counted and converted into a points cloud by Amira. Movies were generated using Amira.

Image registration. Image registration was performed using Elastix toolbox^{66,67} and MelastiX MATLAB wrapper (https://github.com/raacampbell/matlab_elastix). Four different methods of image

registration (Rigid, Similarity, affine and B-Spline) were sequentially performed to register sample data. First, we acquired reference brain images (P28 and P10) stained with Neurotrace 640/660 (N21483, Thermo Fisher Scientific). Second, we transformed the reference brain image to Allen Brain Atlas (developing mouse, P56 and P14, June 2013 v.2) using the Neurotrace 640/660 channel and obtained an autofluorescent image registered to Allen Brain Atlas (AutoF Allen brain atlas). Third, immunostained brain images were registered to the AutoF Allen Brain Atlas using the autofluorescence channel of the immunostained brain.

Electron microscopy

Immunoperoxidase staining for electron microscopy. Three YARG P13 female pups were anesthetized with a mixture of ketamine and xylazine (80 and 10 mg per kg (body weight), intraperitoneal) and were transcardially perfused with PBS (50 mM, pH 7.4), followed by 3.5% acrolein and 4% paraformaldehyde. Brains were cut in ice-cold PBS and stored at -20°C in cryoprotectant until further processing⁶⁸. Brain sections selected in the BF (bregma 0.38 mm to 0.02 mm) were rinsed in PBS, incubated in 0.1 M citrate buffer for 40 min at 70°C for antigen retrieval and quenched with 0.3% hydrogen peroxide for 5 min, followed by treatment with 0.1% sodium borohydride for 30 min. Sections were washed in PBS and blocked in 10% donkey serum with 0.03% Triton X-100 in PBS for 1 h at room temperature and were incubated overnight with anti-ARG1. The next day, sections were rinsed in TBS (50 mM, pH 7.4) and incubated with a secondary antibody conjugated to biotin and with a Vectastain avidin–biotin complex staining kit (Vector Laboratories). Sections were developed in a Tris buffer solution (50 mM, pH 8.0) containing 0.05% diaminobenzidine and 0.015% hydrogen peroxide and rinsed with phosphate-buffered solution (100 mM, pH 7.4). Sections were postfixed with 1% osmium tetroxide, dehydrated using sequential alcohol baths, treated with propylene oxide and embedded in Durcupan resin between fluoropolymer sheets at 55°C for 3 d, as described previously⁶⁹. After ultrathin section generation, microglia positive and negative for ARG1 were imaged and photographed. For information about antibodies, material, reagents and hardware used, see Supplementary Table 2.

Ultrastructural analysis. Ultrastructural analysis was performed using QuPath software (10–11 ARG1⁺ cells and 9–11 ARG1⁻ cells per animal; $n = 3$ animals). Microglial contacts with cell bodies belonging to other brain cells and compartments, including blood vessels, were quantified. Microglia were identified by their heterogenous euchromatin and heterochromatin pattern, electron-dense cytoplasm and distinctive organelles, such as their frequent long stretches of endoplasmic reticulum and lipidic inclusions (that is, lysosomes and lipid droplets)^{70,71}. Microglia were classified as ARG1⁺ or ARG1⁻ depending on the presence (cytoplasmic electron-dense peroxidase precipitate) or absence of immunohistochemistry against ARG1 (complete absence or faint peroxidase precipitate near the cytoplasmic membrane while most of the cytoplasm remained unstained).

Neuronal cell bodies were identified by their electron-lucent cytoplasm and nuclei, often with distinct nucleoli, together with the presence of apical dendrites and axon terminal innervation. Axon terminals were identified by the presence of synaptic vesicles, while dendritic spines were positively identified based on their contact with an axon terminal and the presence of a postsynaptic density. A contact with a synaptic cleft was considered when microglia simultaneously contacted both the axon terminal and dendritic spine forming a synapse⁷⁰. Astrocytic cell bodies were identified by their electron-lucent nuclei characterized by a heterochromatin pattern with a thin electron-dense rim along the nuclear membrane and electron-lucent cytoplasm often containing intermediate filaments. Blood vessels were identified by empty space framed by a basement membrane and underlying pericytes and endothelial cells with tight junctions⁷¹. Contacts with blood vessels were considered when microglial cell bodies were in direct

contact with the basement membrane of the blood vessel. Proximity to blood vessels was considered when microglia were contacting an astrocytic process directly adjacent to the basement membrane⁷⁰. Both types of interactions with vessels were analyzed together. Microglial mitochondria, endoplasmic reticulum, Golgi apparatus, lysosomes and phagocytic inclusions were quantified. Mitochondria were classified as holy mitochondria when they presented a circular empty space contained within their membranes⁷². Phagocytic inclusions were classified by the nature of their contents, that is, empty if the interior of the inclusion was clear, with an axon terminal when synaptic vesicles were identified within the inclusion and with content if the vesicle had content of another nature. Lysosomes were identified by their dark color with heterogenous content contained within a single membrane. Primary and secondary lysosomes were discriminated by the presence of fused endosome vesicles in secondary lysosomes versus an absence in primary lysosomes^{71,73,74}. Nuclear indentations were identified by an invagination of the nuclear membrane^{71,75}.

RNA-seq and RT–qPCR

Microglia isolation. Brains from three to five P13 YARG female or male mice were perfused with 10 ml of cold PBS. The olfactory bulb was removed, and the two hemispheres were separated. Next, the median plane of each hemisphere was placed facing upward, a cut was made posterior to the lateral ventricle, and the tissue ventral to the corpus callosum (including the cerebral nucleus) was dissected out. Tissues were pooled, minced with a scalpel, further dissociated with mechanical dissociation using a tissue grinder on ice (for RNA-seq analysis) and thereafter filtered through 70- μm nylon mesh. The microglial fraction was enriched by a 20% Percoll density gradient at 4°C . For information about reagents used, see Supplementary Table 2.

FACS. The microglial population was initially gated based on size and granularity, followed by gating for singlets, negative selection with CD206–BV421 to exclude macrophages and positive selection with CX3CR1–APC. Finally, microglia were sorted to ARG1⁺ and ARG1⁻ based on YFP expression using a FACSAria III cell sorter system and analyzed using FACSDiva software (BD Biosciences). Cell populations (ARG1–YFP⁺CX3CR1⁺CD206⁻, ARG1–YFP⁻CX3CR1⁺CD206⁻ and CD206⁺) were collected directly in Qiazol (Qiagen). For information about antibodies used, see Supplementary Table 2.

RNA isolation and RT–qPCR. RNA was isolated using commercial kits (RNeasy micro). cDNA was synthesized using oligo d(T), dNTPs and Superscript III (Invitrogen). RT–qPCR was performed using a StepOne Plus instrument (Applied Biosystems) with SYBR Green master mix (Life Technologies) and predesigned primers (KiCqStart Primers, Sigma). Relative gene expression levels were normalized to *Actb* in each sample with the $\Delta\Delta C_t$ method. For information about reagents used, see Supplementary Table 2.

Library preparation and RNA-seq. cDNA was prepared using a SMART-Seq v4 Ultra Low Input RNA kit for sequencing (Takara Bio, 634898). The cDNA quality was examined on an Agilent TapeStation system using a High-Sensitivity D5000 ScreenTape (Agilent, 5067-5592). One nanogram of cDNA was used for library preparation using a Nextera XT DNA library preparation kit (Illumina, FC-131-1024 and FC-131-1096). The yield and quality of the amplified libraries were analyzed using Qubit (Thermo Fisher) and the Agilent TapeStation. The indexed cDNA libraries were normalized and combined, and the pools were sequenced on an Illumina NextSeq 550 for a 75-cycle v2 sequencing run generating 75-base pair single-end reads.

RNA-seq data and computational analysis. Basecalling and demultiplexing were performed using Illumina bcl2fastq v2.20.0 software with default settings, generating fastq files for further downstream mapping

and analysis. Reads were aligned to the Ensembl GRCm38/mm10 reference genome using STAR v2.6.1d. Gene counts were estimated using featureCounts (v1.5.1). Normalization and sample group comparisons of gene counts were performed using the R package DESeq2 (v1.28.1). No filtering was performed before sample group comparisons, where the default DESeq2 independent filtering was applied. For the 'positive versus negative' comparison, a volcano plot was created in GraphPad Prism, which displayed significance and FC for the dataset together with gene symbols for the most highly regulated genes. A heat map for validated genes found to be differentially expressed (up- or down-regulated by at least twofold) between the two microglial populations of interest was generated using GraphPad Prism.

Behavior tests

The experimental mice were subjected to the following described series of behavioral paradigms.

Open field. The open field test was used to assess both exploratory behavior and locomotor activity. Mice were placed for 5 min in an open field ($45 \times 45 \times 45 \text{ cm}^3$). Monitoring was performed with an automated tracking system (SMART 2.5, Panlab). The behavioral parameters registered during 5-min sessions were the percentage of distance travelled in border and center zones, and, to measure a possible anxiety behavior, we calculated the time spent, in percent, in a border zone (*Arg1*-control, $n = 10$ females and $n = 8$ males; *Arg1*-cKO, $n = 9$ females and $n = 6$ males).

Object recognition memory. The object recognition task was used for assessing recognition memory, taking advantage of the ability to discriminate the familiarity of previously met objects. Mice were tested as described previously⁷⁶. Briefly, female mice were placed in a cubic arena ($45 \times 45 \times 45 \text{ cm}^3$) with two identical objects, which they were allowed to explore for 15 min (training phase). One hour later, animals were exposed again to two objects, one familiar and one novel, for 10 min. The number of approximations to exploring the novel object compared to the number of explorations of the familiar object assessed the animal's short-term memory (10 min). Twenty-four hours later, animals were exposed again to two objects, a familiar one and a new one, for 10 min, assessing the animal's long-term memory. The relative exploration of the novel object was expressed as a discrimination index (number novel – novel familiar)/(number novel + number familiar), taking into account the training index (*Arg1*-control, $n = 10$; *Arg1*-cKO, $n = 8$).

Y maze. The Y maze is a test to investigate spatial memory. The maze was made of methacrylate, and each arm was 18 cm long, 38 cm high and 8 cm wide and positioned at equal angles. Working memory was assessed by recording spontaneous exploring behavior in a Y maze. The mice were placed in the center of the maze and allowed to freely explore for 9 min. In this training, we measured the spontaneous alternation triplet and the total number of entries in each arm. To study spatial memory, we used the novel arm discrimination task based on the innate preference of rodents to explore a novel environment more than a familiar one. Therefore, we blocked a specific arm for 5 min. After 1 h, the animals were placed again in the maze with all three arms opened and allowed to explore the familiar arms and the novel arm for 4 min. The percentage of entries in each arm in relation to the percentage of the first session was scored. The whole session was recorded by video and analyzed later using SMART 2.5, Panlab (*Arg1*-control, $n = 11$ females and $n = 8$ males; *Arg1*-cKO, $n = 9$ females and $n = 6$ males).

Rotarod. The rotarod was used to assess motor learning and neuromuscular coordination. To habituate mice to the rotarod (Ugo Basile Biological Research Apparatus), the animals were placed on the roller at a speed of 20 r.p.m. until they could remain on it for 1 min without falling off. To assay motor coordination, mice were tested as

described previously⁷⁷. Briefly, animals were tested at a rotational speed of 20 r.p.m., accelerating to 60 r.p.m. in increments of 5 r.p.m. during four successive trainings and quantifying the latency of the first fall and the number of total falls. Finally, the next day, the protocol was repeated as a final test to estimate the motor memory in all experimental groups (*Arg1*-control, $n = 10$ females and $n = 8$ males; *Arg1*-cKO, $n = 9$ females and $n = 6$ males).

Electrophysiology

For electrophysiological recordings, 2-month-old male and female mice were used.

Slice preparation. Hippocampal slices were prepared as described in detail elsewhere^{78,79}. Mice were anesthetized with isoflurane (2%) and decapitated for slice preparation. Briefly, after decapitation, the whole brain, containing the two hippocampi, was removed into ice-cold solution (I), positioned on the stage of a vibratome slicer and cut to obtain transverse hippocampal slices (350 μm thick), which were maintained continuously oxygenated for at least 1 h before use. All experiments were performed at near-physiological temperatures (31–33 °C). For experiments, slices were continuously perfused with the solution described above. For composition about reagents used, see Supplementary Table 2.

Electrophysiological recordings. fEPSPs were recorded in the CA1 region of the hippocampus and were evoked by a stimulating electrode placed on the Schaffer collaterals (0.2 Hz). Extracellular recording electrodes were filled with solution I. Stimulation was adjusted to obtain an fEPSP amplitude of approximately 0.2 mV under control conditions. In paired-pulse experiments, two consecutive stimuli separated by 40 ms were applied. Data were filtered at 3 kHz and acquired at 10 kHz. A stimulus–response curve (0.1–0.6 mA, mean of five fEPSPs at each stimulation strength) was compiled for the different mice used.

Plasticity protocol. After a stable fEPSP baseline period of 10 min, LTP was induced by a protocol consisting of two trains of stimuli at 100 Hz, 1 s separated by 20 s. Recordings lasted 60 and 120 min after the application of the protocol.

Data analysis. Data were analyzed using Clampfit 10.2 software (Molecular Devices). The last 10 min of recording were used to estimate changes in synaptic efficacy compared to baseline. The PPR was expressed as the slope of the second fEPSP divided by the slope of the first fEPSP. Data are presented as mean \pm s.e.m. Statistical comparisons were made using Student's *t*-tests. *P* values less than 0.05 were considered statistically significant.

Statistical analysis

All statistical analyses were conducted using Prism 8 (v.9.3.1, GraphPad Software) and Stata (v 17.0, StataCorp). Results are presented as the mean \pm s.e.m. Data normality was tested using the Shapiro–Wilk test. For normally distributed data, differences in means between groups were examined using two-tailed paired or unpaired Student's *t*-tests or analysis of variance, whichever was appropriate. For data that were not normally distributed, a Wilcoxon signed-rank test for paired data, a Mann–Whitney *U*-test or a Kruskal–Wallis test was used. Differences were considered statistically significant if *P* values were less than 0.05. Raw data are available as Source Data.

Statistics and reproducibility

All experimental studies are guided by the 3R principle, EU Directive 2010/63/EU. The investigators were blinded to the conditions of the experiments during data collection and quantification. No statistical methods were used to predetermine sample sizes, but these are consistent with previous publications^{78–83}. No data points have been excluded. We excluded

animals without mobility in both groups. These exclusion criteria were preestablished. Animals were randomly assigned to two groups based on genotype and were further subdivided by gender for behavioral studies. For morphometric and manual counting analyses, sample IDs were randomized using an Excel-generated randomized numerical ID.

Reporting summary

Further information on research design is available in the Nature Portfolio Reporting Summary linked to this article.

Data availability

The bulk RNA-seq data that support the findings of this study are available at Gene Expression Omnibus under accession number [GSE216893](https://www.ncbi.nlm.nih.gov/geo/query/acc.cgi?acc=GSE216893). Source data are provided with this paper. All other data are available from the corresponding authors upon request.

References

60. Carrillo-Jimenez, A. et al. TET2 regulates the neuroinflammatory response in microglia. *Cell Rep.* **29**, 697–713 (2019).
61. Ativie, F. et al. Cannabinoid 1 receptor signaling on hippocampal GABAergic neurons influences microglial activity. *Front. Mol. Neurosci.* **11**, 295 (2018).
62. Renier, N. et al. iDISCO: a simple, rapid method to immunolabel large tissue samples for volume imaging. *Cell* **159**, 896–910 (2014).
63. Tomer, R., Ye, L., Hsueh, B. & Deisseroth, K. Advanced CLARITY for rapid and high-resolution imaging of intact tissues. *Nat. Protoc.* **9**, 1682–1697 (2014).
64. Schindelin, J. et al. Fiji: an open-source platform for biological-image analysis. *Nat. Methods* **9**, 676–682 (2012).
65. Bria, A. & Iannello, G. TeraStitcher—a tool for fast automatic 3D-stitching of teravoxel-sized microscopy images. *BMC Bioinformatics* **13**, 316 (2012).
66. Klein, S., Staring, M., Murphy, K., Viergever, M. A. & Pluim, J. P. elastix: a toolbox for intensity-based medical image registration. *IEEE Trans. Med. Imaging* **29**, 196–205 (2010).
67. Shamonin, D. P. et al. Fast parallel image registration on CPU and GPU for diagnostic classification of Alzheimer’s disease. *Front. Neuroinform.* **7**, 50 (2013).
68. Tremblay, M. E., Riad, M. & Majewska, A. Preparation of mouse brain tissue for immunoelectron microscopy. *J. Vis. Exp.* **41**, e2021 (2010).
69. Bisht, K., El Hajj, H., Savage, J. C., Sánchez, M. G. & Tremblay, M. Correlative light and electron microscopy to study microglial interactions with β -amyloid plaques. *J. Vis. Exp.* **112**, e54060 (2016).
70. Peters, A., Palay S. L. & Webster H. D. *The Fine Structure of the Nervous System: Neurons and Their Supporting Cells* 3rd edn. (Oxford Univ. Press, 1991).
71. Nahirney, P. C. & Tremblay, M. E. Brain ultrastructure: putting the pieces together. *Front. Cell Dev. Biol.* **9**, 629503 (2021).
72. Miyazono, Y. et al. Uncoupled mitochondria quickly shorten along their long axis to form indented spheroids, instead of rings, in a fission-independent manner. *Sci. Rep.* **8**, 350 (2018).
73. Holtzman, E., Novikoff, A. B. & Villaverde, H. Lysosomes and GERL in normal and chromatolytic neurons of the rat ganglion nodosum. *J. Cell Biol.* **33**, 419–435 (1967).
74. Nandy, K. Properties of neuronal lipofuscin pigment in mice. *Acta Neuropathol.* **19**, 25–32 (1971).
75. Henry, M. S. et al. Delta opioid receptor signaling promotes resilience to stress under the repeated social defeat paradigm in mice. *Front. Mol. Neurosci.* **11**, 100 (2018).
76. Cubillos-Rojas, M. et al. The HERC2 ubiquitin ligase is essential for embryonic development and regulates motor coordination. *Oncotarget* **7**, 56083–56106 (2016).
77. Bachiller, S. et al. The HERC1 E3 ubiquitin ligase is essential for normal development and for neurotransmission at the mouse neuromuscular junction. *Cell. Mol. Life Sci.* **72**, 2961–2971 (2015).
78. Falcón-Moya, R. et al. Astrocyte-mediated switch in spike timing-dependent plasticity during hippocampal development. *Nat. Commun.* **11**, 4388 (2020).
79. Pérez-Rodríguez, M. et al. Adenosine receptor-mediated developmental loss of spike timing-dependent depression in the hippocampus. *Cereb. Cortex* **29**, 3266–3281 (2019).
80. Boza-Serrano, A. et al. Galectin-3, a novel endogenous TREM2 ligand, detrimentally regulates inflammatory response in Alzheimer’s disease. *Acta Neuropathol.* **138**, 251–273 (2019).
81. Suárez-Pereira, I. et al. The absence of caspase-8 in the dopaminergic system leads to mild autism-like behavior. *Front. Cell Dev. Biol.* **10**, 839715 (2022).
82. García-Domínguez, I. et al. Selective deletion of caspase-3 gene in the dopaminergic system exhibits autistic-like behaviour. *Prog. Neuropsychopharmacol. Biol. Psychiatry* **104**, 110030 (2021).
83. Suárez-Pereira, I. & Carrión, Á. Updating stored memory requires adult hippocampal neurogenesis. *Sci. Rep.* **5**, 13993 (2015).
84. McKinsey, G. L. et al. A new genetic strategy for targeting microglia in development and disease. *eLife* **9**, e54590 (2020).

Acknowledgements

We thank the Bioinformatics and Expression Analysis core facility, the Biomedicum Flow Cytometry core facility and the Biomedicum Imaging core facility (with grants from the Strategic Research Area in Neuroscience (StratNeuro) and the Strategic Research Area in Stem Cells and Regenerative Medicine (StratRegen) supported by the Swedish government) at the Karolinska Institutet for technical support. We would like to thank S. Vazquez and B. Ben-Azu for technical support. We are grateful to P.C. Nahirney for the use of a transmission electron microscope and B. Gowen for technical assistance. This research is supported by the Swedish Research Council and the Swedish Brain Foundation (P.U. and B.J.), the Sigrid Jusélius Foundation, the Svenska Kulturfonden and Academy of Finland (33552, V.S.), the Swedish Cancer Foundation (P.U. and B.J.), the Swedish Cancer Society (K.G., P.U. and B.J.), the Karolinska Institutet Foundation (P.G.-R. and B.J.), the Mexican Council of Science and Technology (F.G.I.), the Fonds de recherche du Québec—Santé (K.P.), the Wenner-Gren Foundation (K.G.), the Åke Wibergs Stiftelse (M.C.), the Spanish Ministerio de Ciencia e Innovación/FEDER/UE PID2021-124096OB-I00 (J.L.V.), PID 2019-109569GB-I00 (J.A.A.) and BFU2015-68655 (A.R.-M.), the Spanish Junta de Andalucía/FEDER/EU P18-RT-1372 and the Spanish FEDER I+D+I-USE US-1264806 (J.L.V.), the Swedish Childhood Cancer Foundation (K.B., L.K., P.U. and B.J.), the Swedish governmental grants for researchers working in healthcare (K.B.), the Canada Research Chair (Tier 2) in Neurobiology of Aging and Cognition (M.-E.T.), the TraInflam grant from ERA-NET NEURON Neuroinflammation (B.J., M.-E.T. and M.T.H.) and the Academy of Finland (V.S. and M.A.; 309489, 324177). We acknowledge and respect that the University of Victoria is located on the territory of the ɫəkwʷəjən peoples and that the Songhees, Esquimalt and WSÁNEƷ peoples have relationships to this land.

Author contributions

V.S. performed the experiments except otherwise indicated. R.R. performed immunohistochemistry and subsequent analyses. R.R., I.G.-D., I.A.-B., G.V.-C. and J.L.V. developed the *Arg1*-cKO mice, did the behavioral studies and analyzed the generated data. S.K. and P.U. performed iDISCO and subsequent analyses. A.M.O., A.L.-R. and K.B. performed tissue collection and processing and established the

cell isolation protocol. J.A.A. and E.M.P.-V. performed Golgi stainings and subsequent analyses as well as ChAT stainings and subsequent analyses. A.R.-M. and I.M.-G. performed electrophysiological experiments. A.-N.M., G.V.-C. and M.P.-P. performed tissue processing and immunohistochemistry. L.K. and J.A.-C. helped with FACS sorting. F.G.I., K.P., N.V. and M.-E.T. performed and analyzed the transmission electron microscopy data. D.T. and M.T.H. did the morphometric analysis. K.G. and D.B. contributed to RNA-seq data analysis. M.C. and L.K. performed the RNA extraction and RT-qPCR of the cell-sorted samples. M.C. and P.G.-R. were involved in the quantification analysis. M.A. helped with data analysis. Y.C. assisted with statistical analysis. V.S. and B.J. initiated, conceptualized and designed the study, analyzed and interpreted the data and wrote the first draft of the paper. All authors discussed the results and commented or edited the paper.

Funding

Open access funding provided by Karolinska Institute.

Competing interests

The authors declare no competing interests.

Additional information

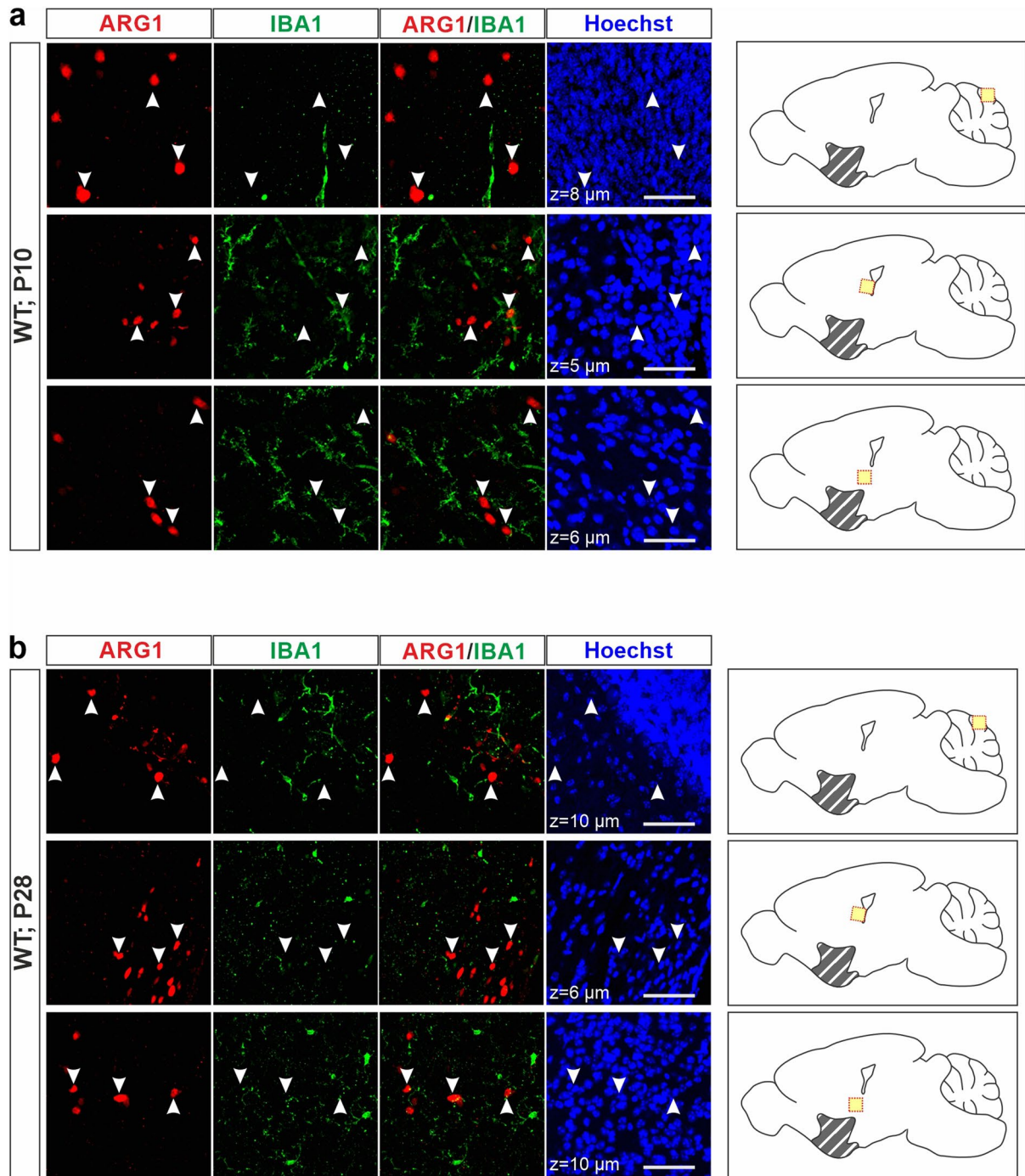
Extended data is available for this paper at <https://doi.org/10.1038/s41593-023-01326-3>.

Supplementary information The online version contains supplementary material available at <https://doi.org/10.1038/s41593-023-01326-3>.

Correspondence and requests for materials should be addressed to Vassilis Stratoulas or Bertrand Joseph.

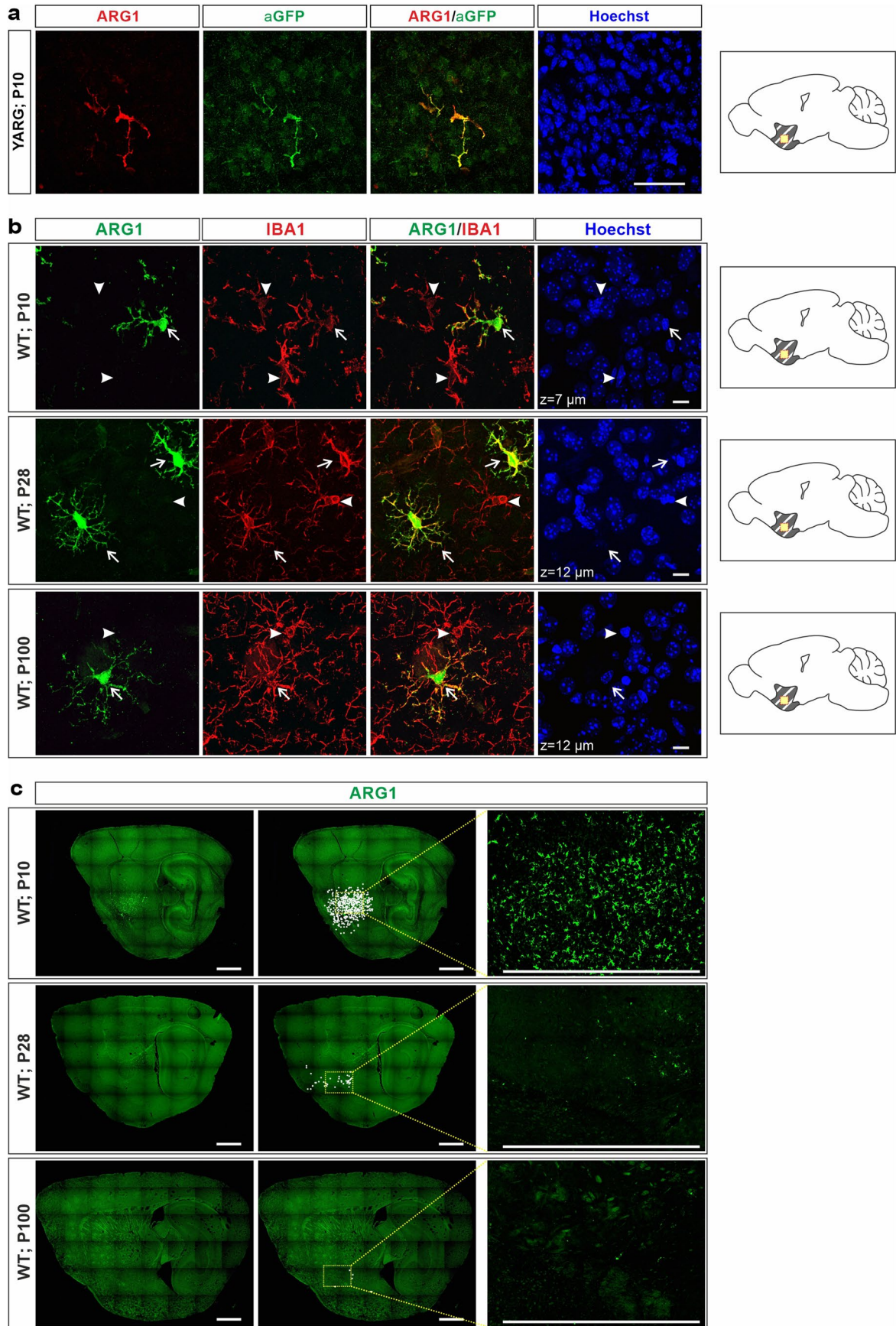
Peer review information *Nature Neuroscience* thanks the anonymous reviewers for their contribution to the peer review of this work.

Reprints and permissions information is available at www.nature.com/reprints.



Extended Data Fig. 1 | ARG1-positive cells that are not microglia in WT mouse brain. a-b. ARG1⁺/IBA1⁻ cells in the cerebellum and around the ventricles (arrowheads) both at P10 (**a**) and at P28 (**b**) (representative images from

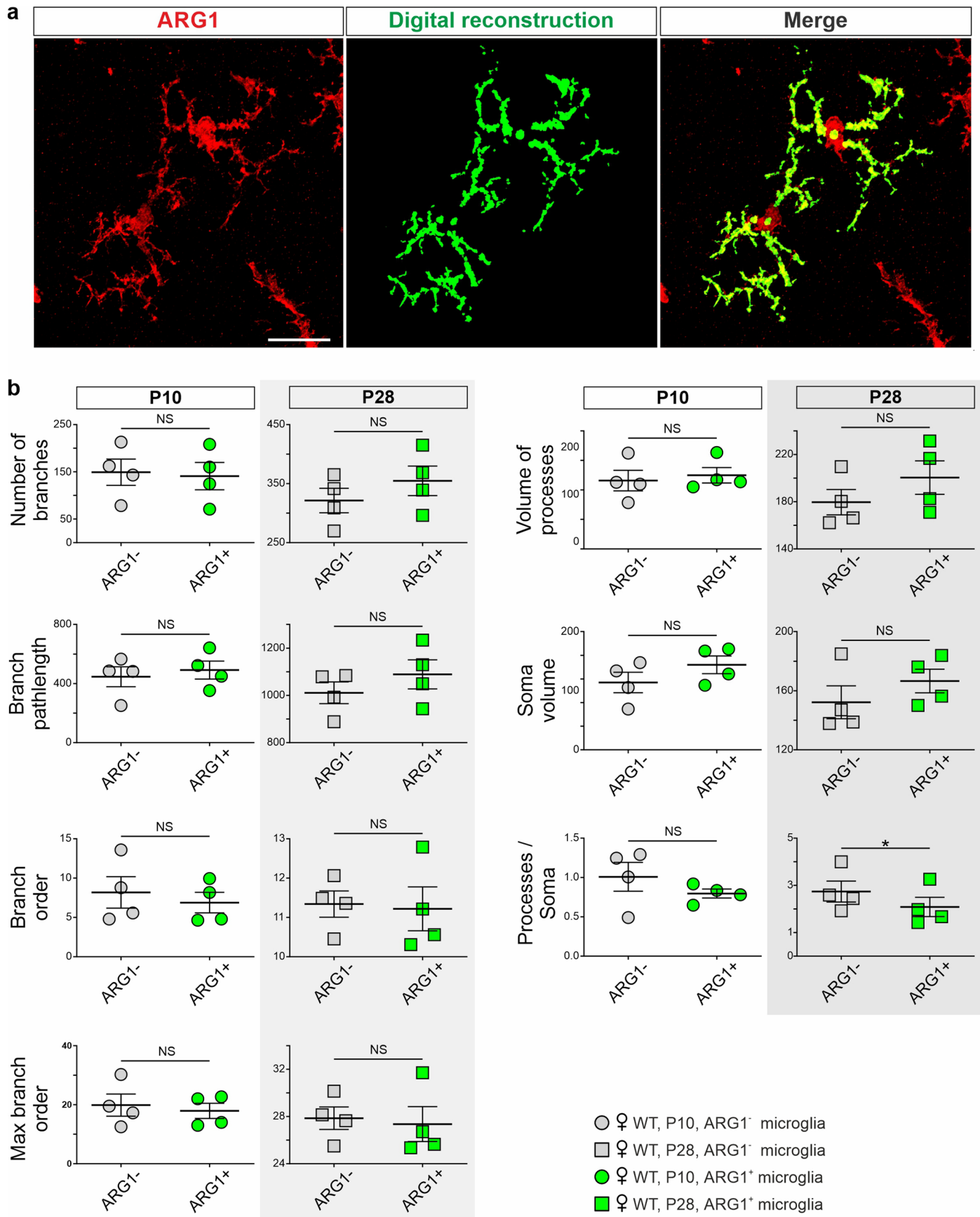
3 female animals per group). Scale bars, x = 50 μm. Yellow squares indicate location of the corresponding images on their left; grey lines indicate the BF/vStr region.



Extended Data Fig. 2 | See next page for caption.

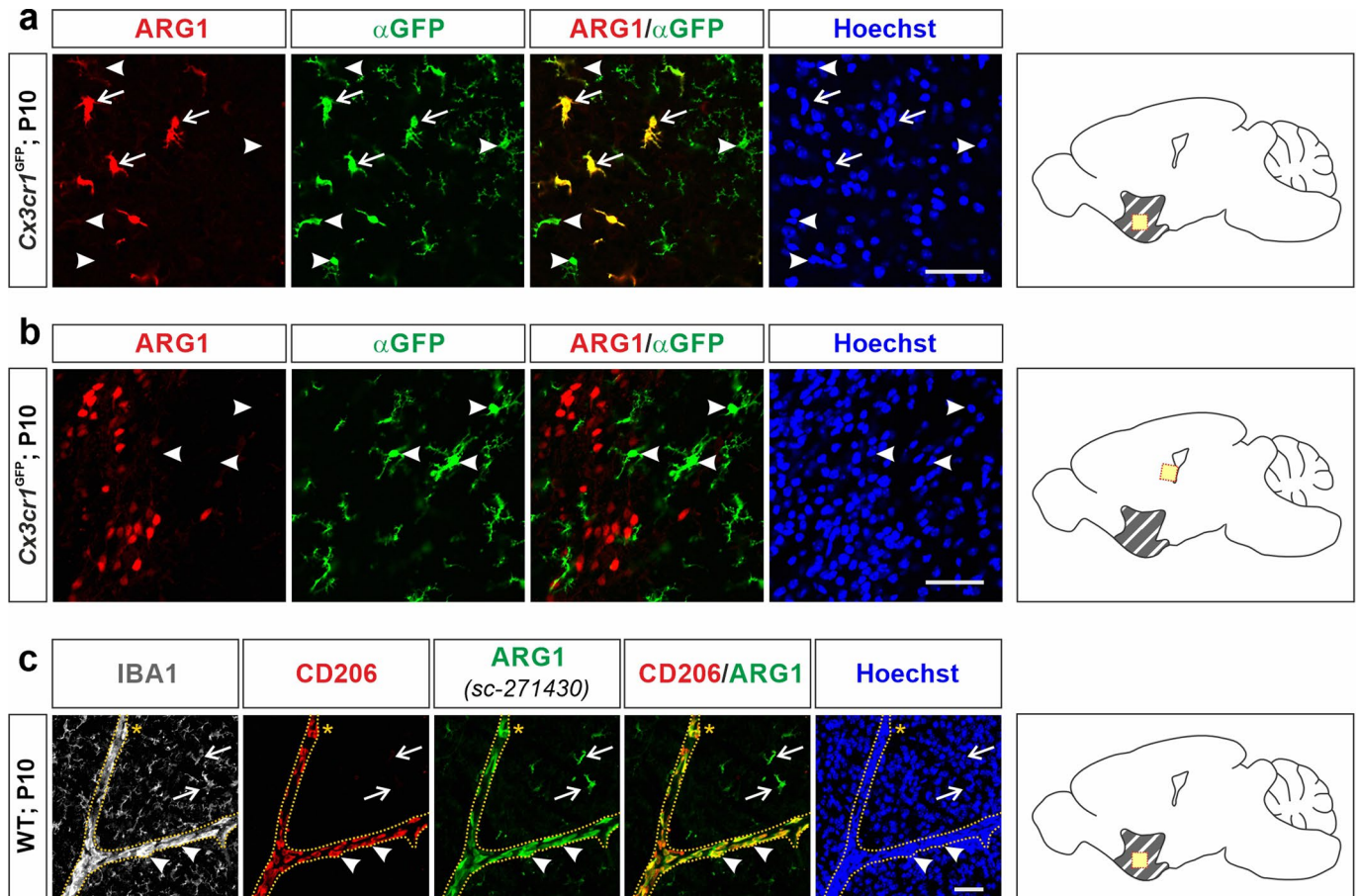
Extended Data Fig. 2 | Arg1+microglia co-exist with Arg1⁻negative-microglia in the same vicinity in P10, P28 and P100 WT mouse brain. **a**, *Arg1*-YFP-positive microglia in male YARG mice, as recognised by α -GFP and α -ARG1 antibodies (representative image from 3 female animals). **b**, Arg1+microglia (arrows) and Arg1-negative-microglia (arrowheads) during mouse brain development.

c, Arg1+microglia in BF/vStr at P10, P28 and P100 (representative images from 3 female animals per group). Each white dot represents a single Arg1+microglia and has been manually annotated. Scale bars, x = 50 μ m, z = 10 μ m (**a**), x = 10 μ m (**b**), x = 1000 μ m, z = 4 μ m (**c**). Yellow squares indicate location of the corresponding images on their left; grey lines indicate the BF/vStr region.



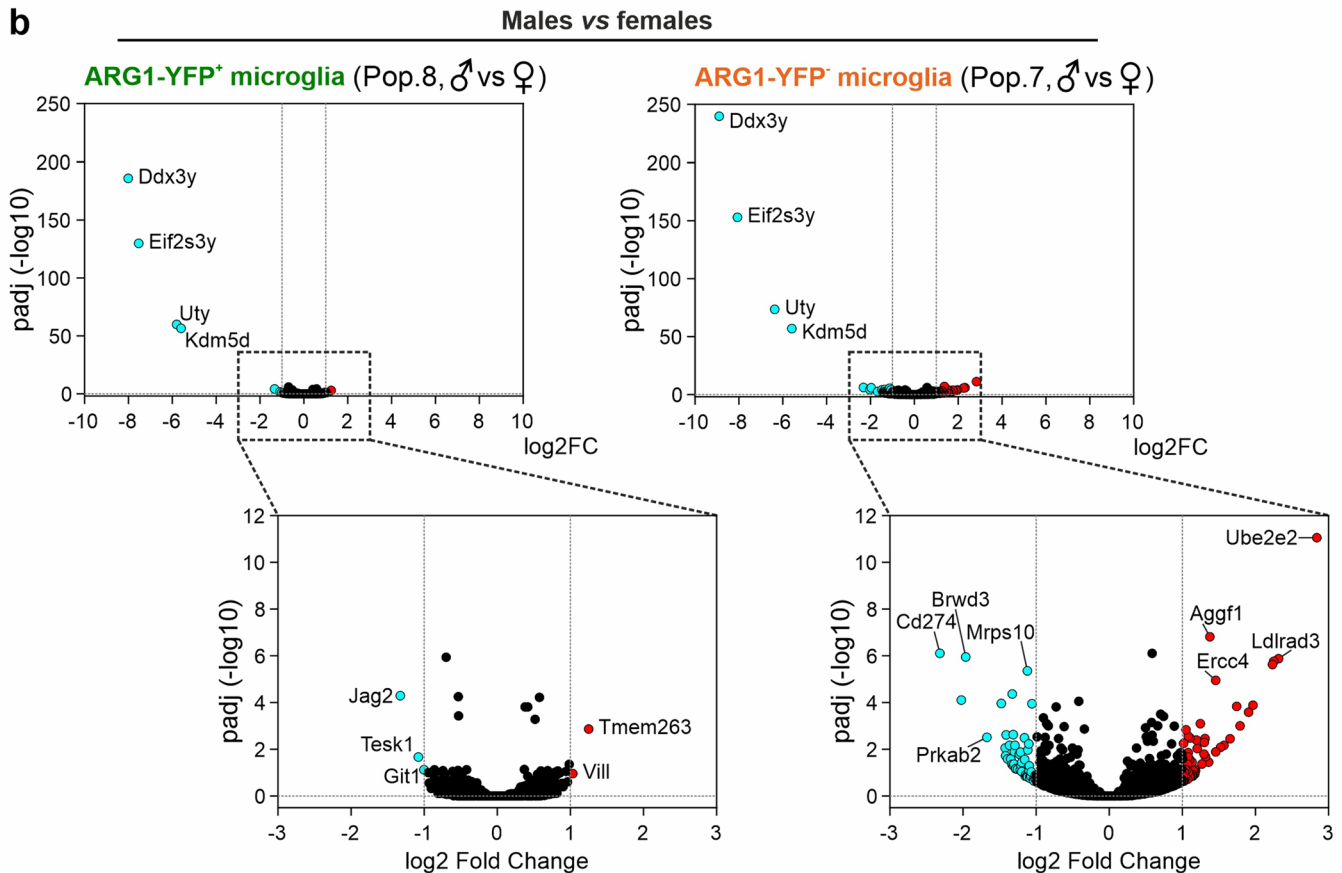
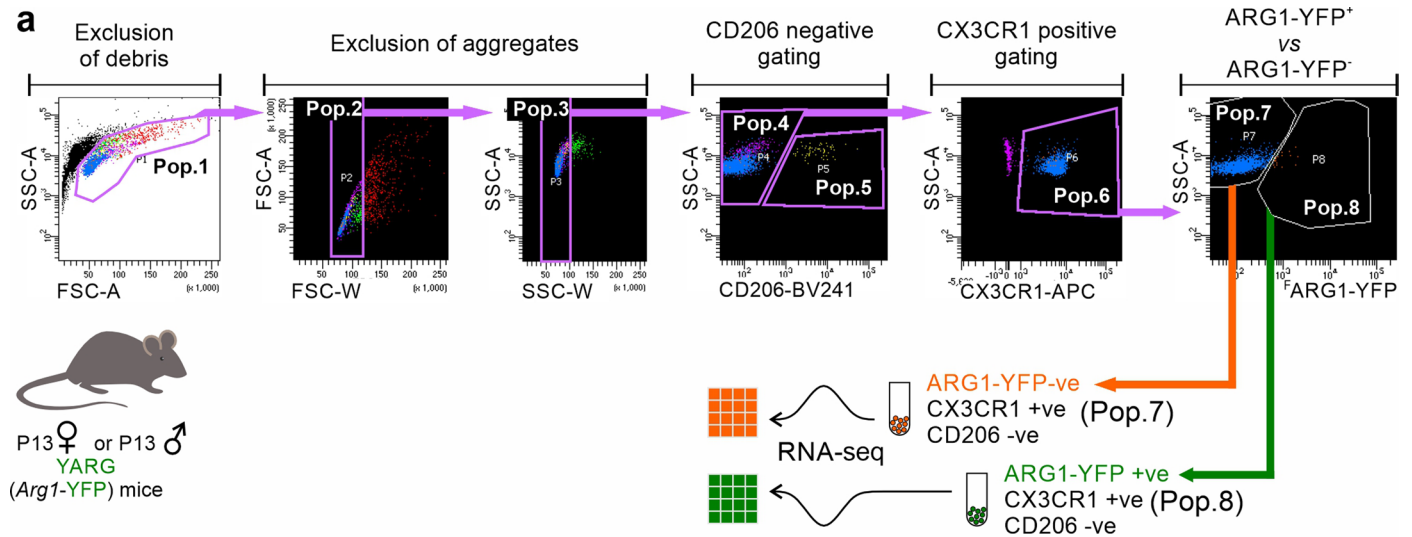
Extended Data Fig. 3 | Morphometric comparison of P10 and P28 Arg1-negative-microglia versus Arg1+microglia from basal forebrain.
a, Illustration of digital reconstruction of two Arg1+microglia. **b**, Morphometric comparisons of Arg1+microglia and Arg1-negative-microglia from P10 and P28

mouse brain. Each circle or square represents data from a single animal (n = 4 female animals per group). P28, Processes/Soma, $P = 0.0259$. Scale bar, $x = 10 \mu\text{m}$, $z = 15 \mu\text{m}$. Data in **b** represented as mean \pm s.e.m. Statistical significances were determined by paired two-sided t tests; * $P < 0.05$, n.s. indicates not significant.



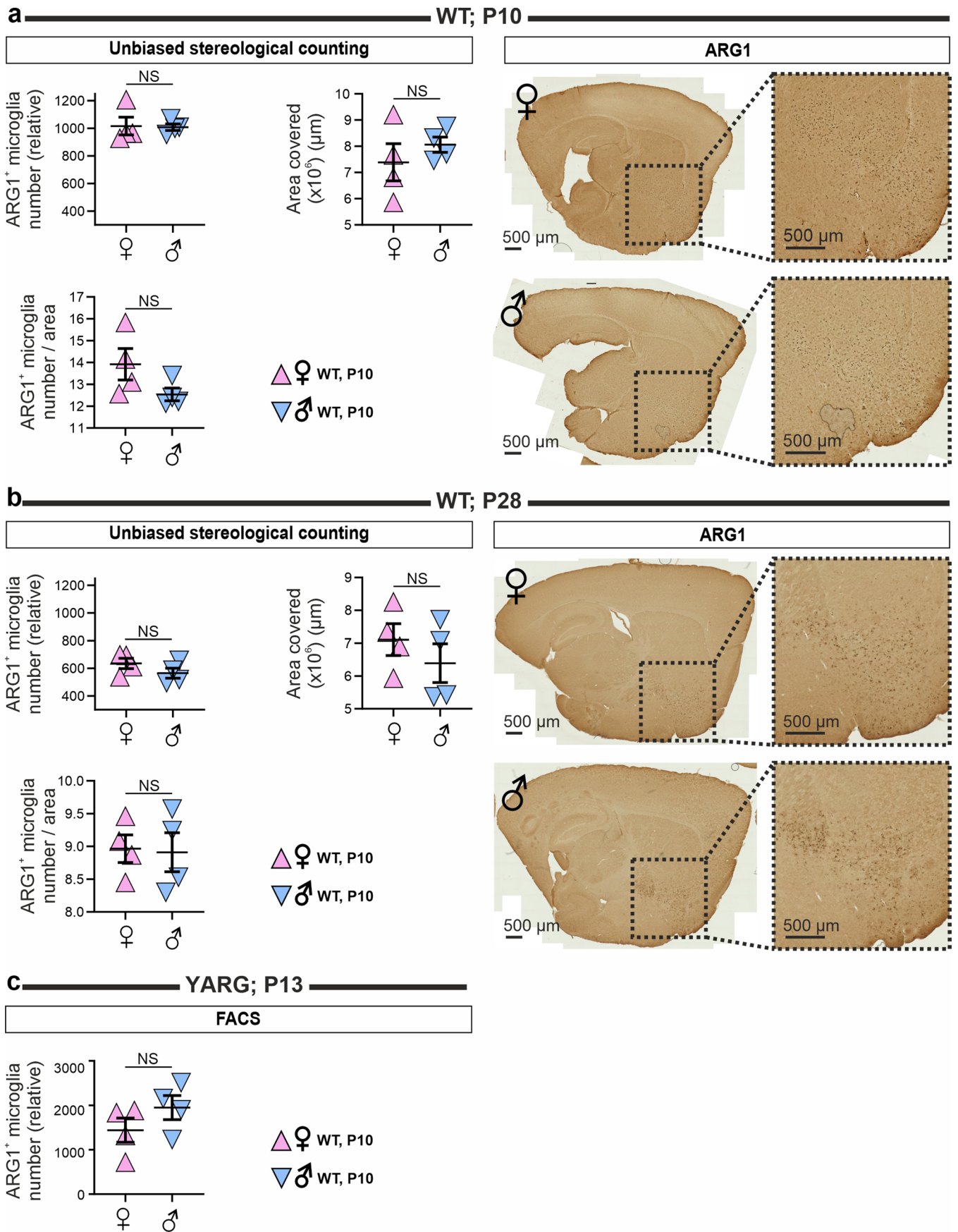
Extended Data Fig. 4 | Arg1+microglia co-localize with CX3CR1-GFP but not with CD206 in P10 mouse brains. a, CX3CR1-GFP⁺/ARG1⁺ microglia (arrows) coexist with CX3CR1-GFP⁺/ARG1⁻ microglia (arrowheads) in P10 BF/vStr (representative image from 3 female animals). **b**, ARG1-positive cells around the ventricles (triple arrows) are not CX3CR1-GFP-positive (see also Extended Data Fig. 1) (representative image from 3 female animals). **c**, Arg1+microglia

do not express the perivascular macrophage marker CD206 (arrows), while perivascular macrophages in this brain area express ARG1 (arrowheads). Note that Arg1+microglia are always ramified, while perivascular macrophages are amoeboid (representative image from 3 female animals). Scale bars, $x = 50 \mu\text{m}$, $z = 10$ and $8.5 \mu\text{m}$ (for **a** and **c**, respectively). Yellow squares indicate location of the corresponding images on their left; grey lines indicate the BF/vStr region.



Extended Data Fig. 5 | P13 Arg1+ microglia from basal forebrain do not have sex-specific signatures. a, Gating strategy for fluorescent-activated cell sorting of ARG1-YFP-positive (population, Pop.8) and ARG1-YFP-negative (Pop.7) microglia. **b**, Volcano plots of differentially expressed genes between males and females in ARG1-YFP-positive (Pop.8) and ARG1-YFP-negative (Pop.7)

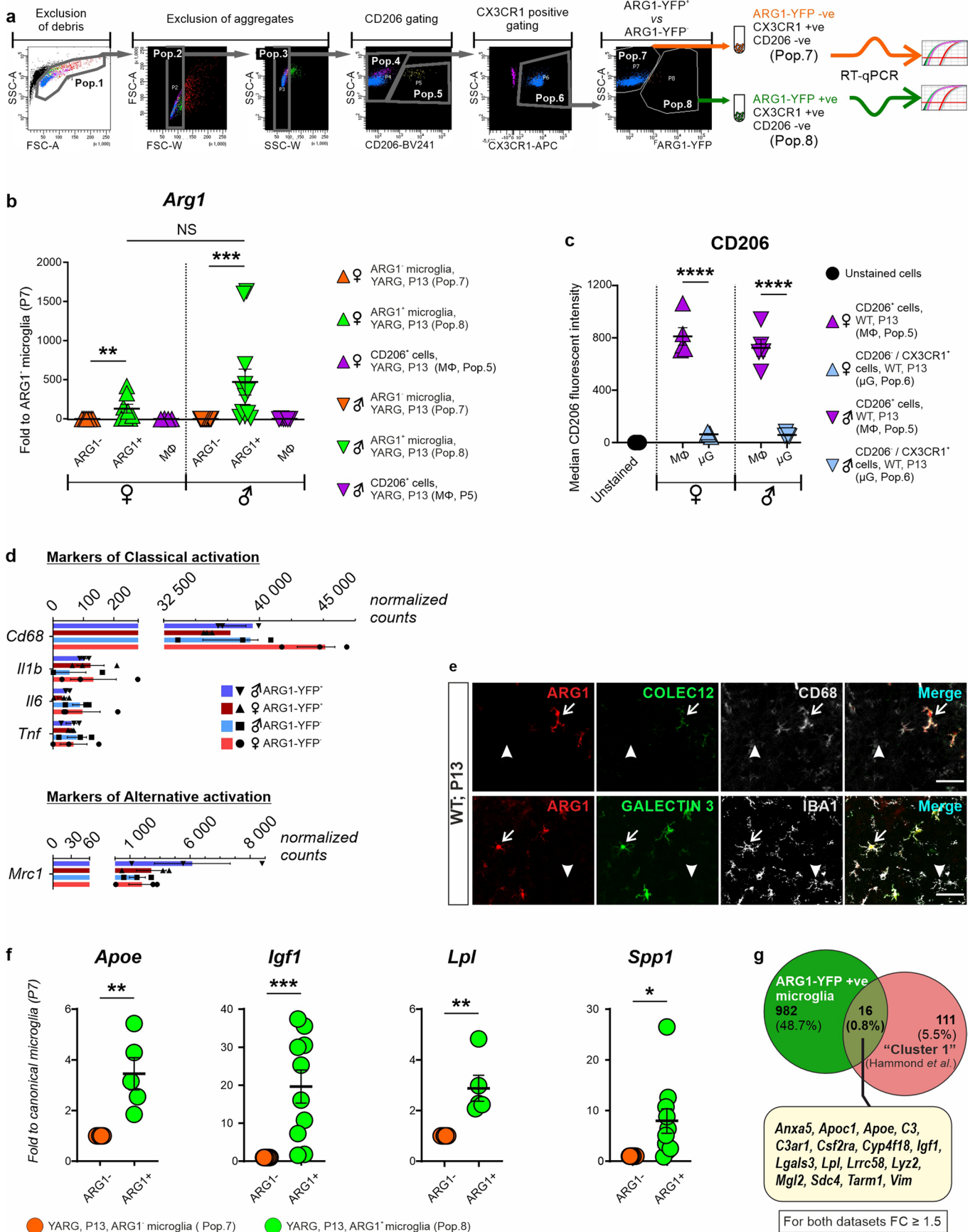
sorted microglia. Three to five brains were dissected from either female or male animals per biological replicate (n = 3 litters per sex). P-values (two-sided) attained by the Wald test are corrected for multiple testing using the Benjamini and Hochberg method.



Extended Data Fig. 6 | See next page for caption.

Extended Data Fig. 6 | P10, P13 and P28 female and male mice do not have notable differences in Arg1+microglia numbers. a-b, Quantification of Arg1+microglia from matching sections of P10 (**a**) and P28 (**b**) wild type animals (n = 4 animals per sex) and representative DAB stainings. **c,** Quantification of ARG1-YFP-positive microglia (Pop.8, as described in Extended Data

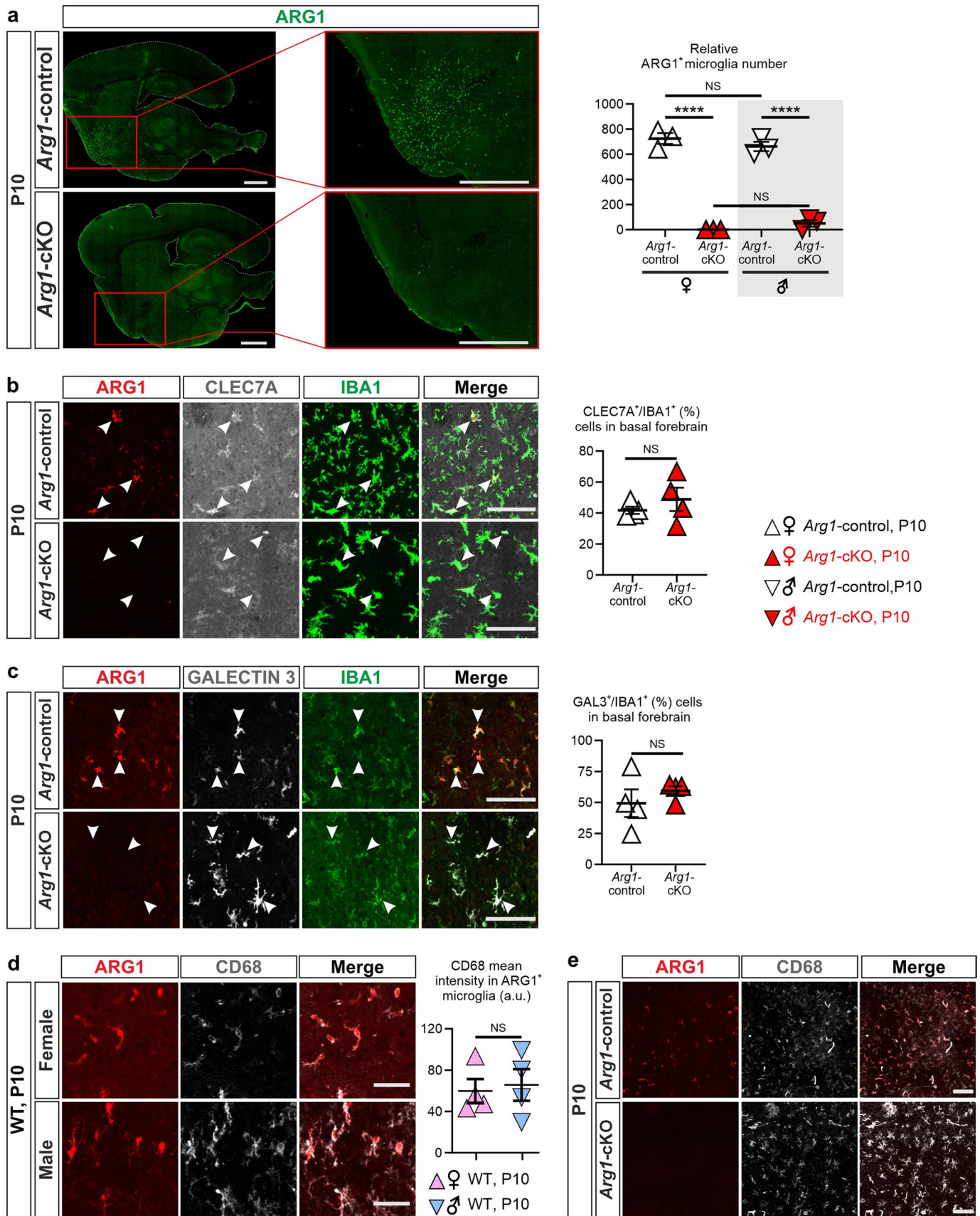
Fig. 5a) from P13 *Arg1*-YFP female and male animals (n = 4 animals per sex). Each arrow corresponds to one animal. Scale bars, 500 μ m. Data represented as mean \pm s.e.m. Statistical significances were determined by two-sided unpaired *t* tests (**a**, **b**, and **c**) or two-sided Mann-Whitney U test (for Arg1+microglia number in **a**). *n.s.* indicates not significant.



Extended Data Fig. 7 | See next page for caption.

Extended Data Fig. 7 | P13 Arg1+microglia cannot be classified as either classical or alternative activated microglia. a, Gating strategy for RT-qPCR was identical to gating for sorting prior to RNA-Seq (Extended Data Fig. 5a). **b**, RT-qPCR indicates that *Arg1* gene expression is restricted to the ARG1-YFP+ / CX3CR1-/CD206⁻ (Pop.8) population. Three to five brains were dissected from either female or male animals per biological replicate (females, n = 8 litters; males, n = 12 litters). Female, ARG1^{negative} - ARG1^{positive}, $P = 0.0096$; male, ARG1^{negative} - ARG1^{positive}, $P < 0.0001$. **c**, Microglia (μ G) are known to express low levels of *Mrc1* (gene expressing CD206) (**a**, reference⁸⁴), in substantially lower levels than macrophages (M Φ) (females, n = 6 litters; males, n = 5 litters). Female, macrophages - microglia, $P < 0.0001$; male, macrophages - microglia, $P < 0.0001$. **d**, Although ARG1 is long been considered a marker of alternative activation, P13 Arg1+microglia (and P13 Arg1-negative-microglia), express

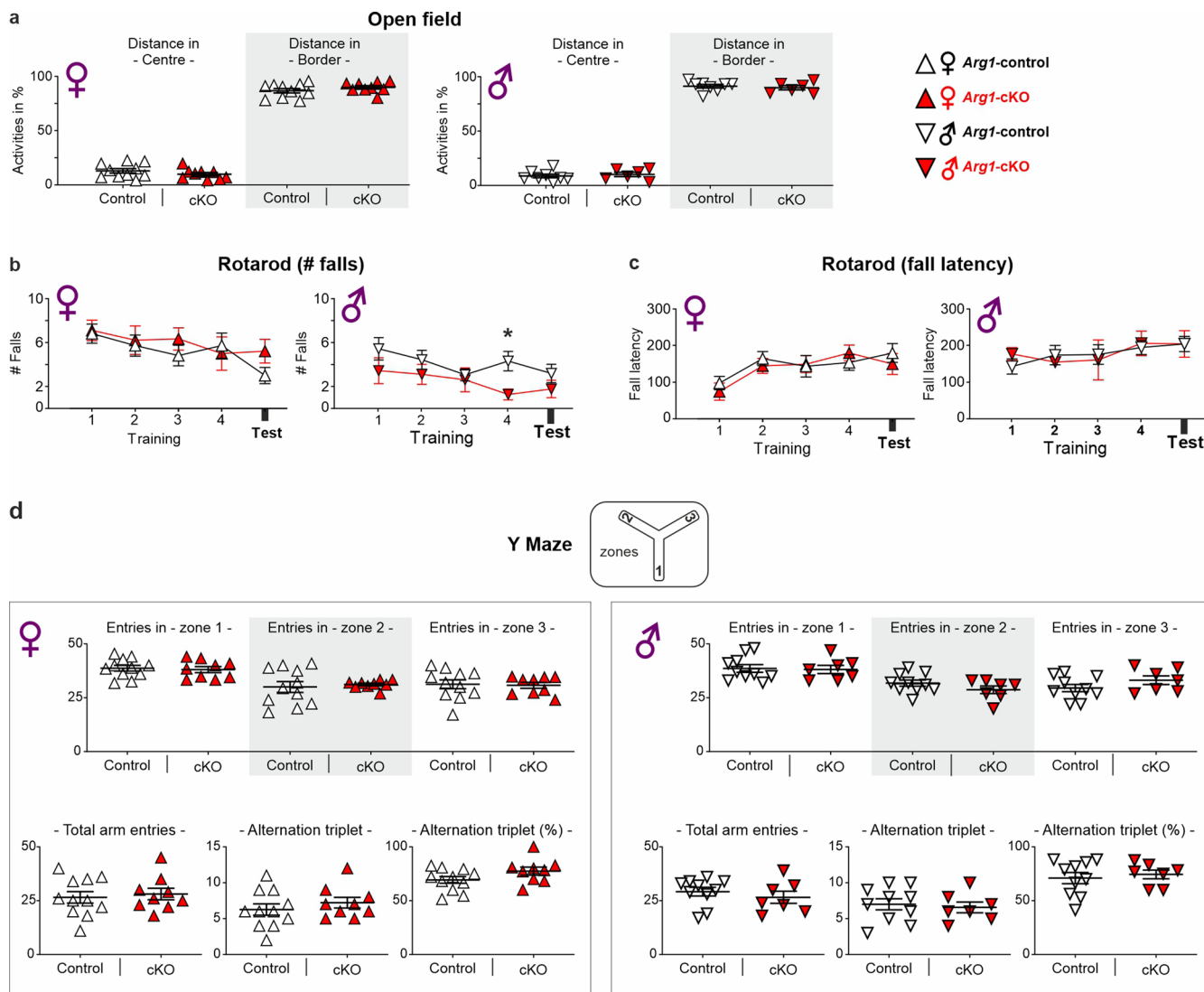
both classical and alternative activation markers (females, n = 3 litters; males, n = 3 litters, data derived from RNA-Seq). **e-f**, Differentially expressed genes from RNA-Seq validated by immunohistochemistry (representative image from 3 female animals) (**e**) and RT-qPCR (n = min. 5 litters) (**f**). *ApoE*, $P = 0.0049$; *Igf1*, $P = 0.0005$; *Lpl*, $P = 0.0062$; *Spp1*, $P = 0.0101$. Scale bars, 50 μ m. **g**, Venn diagram showing overlaps between Arg1+microglia and Arg1-negative-microglia presented here and "cluster 1" (reference¹⁷) ($FC \geq 1.5$). Note: only validated genes have been included in this list. Data in **b**, **c** and **f** are represented as mean \pm s.e.m. Statistical significances were determined by Kruskal-Wallis test (**b**, Arg1), ANOVA (**c**, CD206), and unpaired *t* tests (**f**); all P-values are two-sided, and P-values for multiple comparisons were corrected using Dunn's method (**b**) and Bonferroni's method (**c**), respectively. * $P < 0.05$; ** $P < 0.01$; *** $P < 0.001$; **** $P < 0.0001$, *n.s.* indicates not significant.



Extended Data Fig. 8 | See next page for caption.

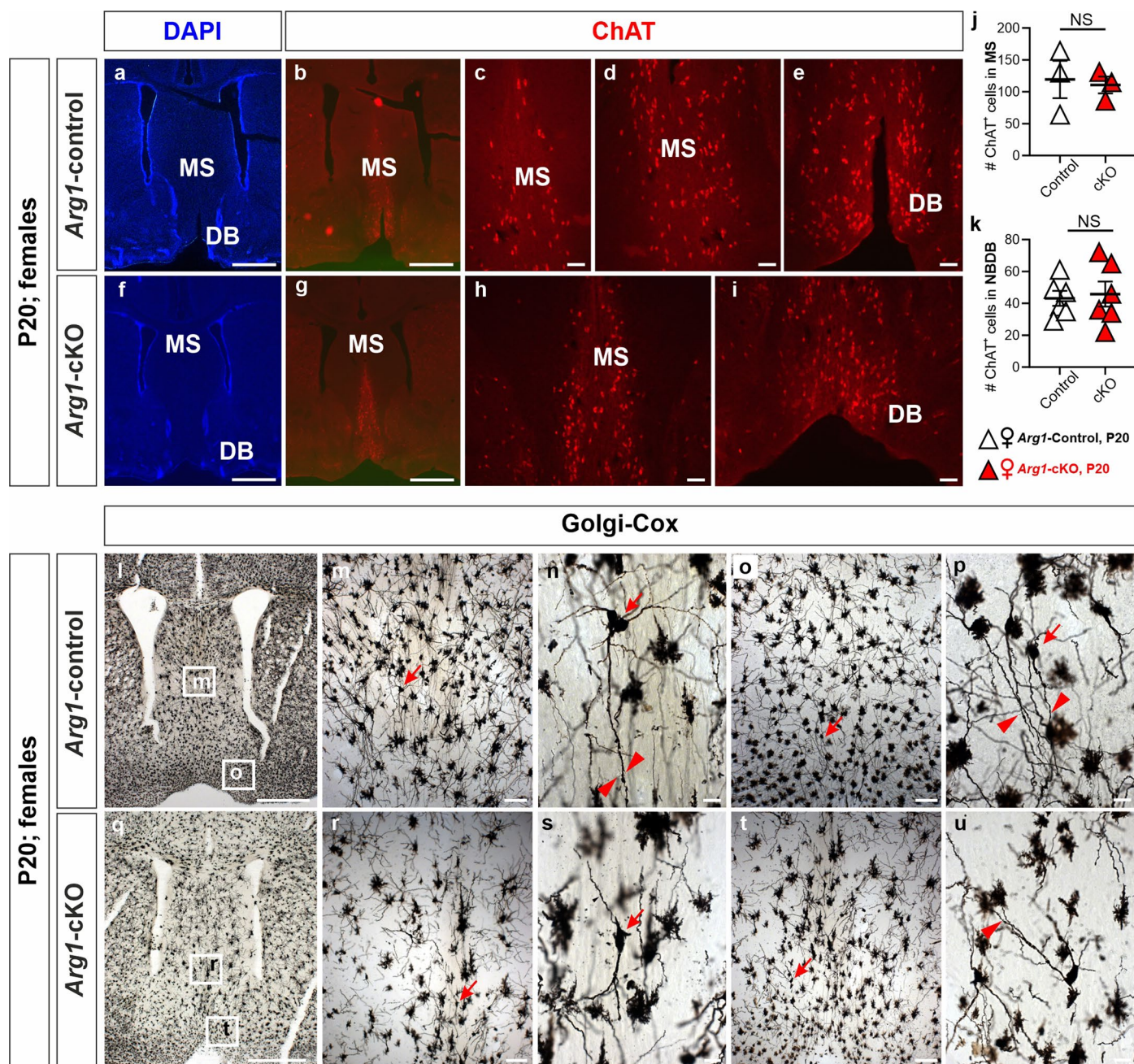
Extended Data Fig. 8 | Arg1+microglia are efficiently knocked down in female and male Arg1-cKO. **a**, Staining of matching sections shows that in *Arg1-cKO* animals, only few Arg1+microglia remain when compared to *Arg1-Control*. Quantification of Arg1+microglia from matching sections ($n = 3$ animals per group). Female, *Arg1^{Control} - Arg1^{cKO}*, $P < 0.0001$; male, *Arg1^{Control} - Arg1^{cKO}*, $P < 0.0001$. Scale bar, $x = 1000 \mu\text{m}$. **b**, Arg1+microglia co-localize with the marker GALECTIN-3, as inferred by our RNA-Seq analysis. Scale bar, $x = 100 \mu\text{m}$, $z = 10 \mu\text{m}$. In *Arg1-cKO* basal forebrain, the percentage of CLEC7A +/IBA1 + cells is not statistically significant different to the percentage of CLEC7A +/IBA1 + cells

in the basal forebrain of *Arg1-Control* animals. **c**, Similar for GALECTIN-3 +/IBA1 + cells. **d**, Mean intensity of the lysosomal marker CD68 in female and male Arg1+microglia in BF. The images in **b**, **c** and **e** are representative of 4 female animals per group. Scale bars, $x = 50 \mu\text{m}$, $z = 5 \mu\text{m}$. **e**, CD68 expression in BF of *Arg1-Control* and *Arg1-cKO* basal forebrain. Scale bars, $x = 100 \mu\text{m}$, $z = 5 \mu\text{m}$. Data in **a-d** are represented as mean \pm s.e.m. Statistically significant differences were determined by ANOVA (**a**), Mann-Whitney U (**b**), or unpaired t tests (**c** and **d**). All P-values are two-sided, and P-values for multiple comparisons were corrected using Bonferroni's method (**a**). **** $P < 0.0001$, *n.s.* indicates not significant.



Extended Data Fig. 9 | *Arg1-cKO* female and male animals do not show motoric phenotypes. a-e, *Arg1-cKO* animals and controls were assessed for motoric (a-c) and memory (d) phenotypes. Each triangle corresponds to one animal. Female *Arg1-Control* n = 10 (a-c), n = 11 (d) and *Arg1-cKO* n = 9 (a-d);

male *Arg1-Control* n = 8 (a-c), n = 10 (d) and *Arg1-cKO* n = 6 (a-c), n = 7 (d). Males, rotarod #falls, training 4, $P = 0.0184$. Data represented as mean \pm s.e.m. Statistically significant differences were determined by unpaired two-sided t tests. * $P < 0.05$.



Extended Data Fig. 10 | P20 female medial septum and Broca's diagonal band do not show differences in number of ChAT positive neurons between Arg1-Control and Arg1-cKO brains. a-i, Microphotographs of coronal sections of *Arg1-Control* (a-e and l-p) and *Arg1-cKO* (f-i and q-u) P20 forebrain. Choline acetyltransferase immunoreactive cells somata are uniformly distributed through the medial septum (MS; b-d and g-h) and the Broca's diagonal band (DB; e and i). j-k, ChAT positive neuron cell count in MS and NBDN did not reveal differences between the two genotypes (j, n = 3 and k, n = 6 animals). l-u, Golgi-Cox method shows the morphology of the neurons of the medial septum (m-n and r-s) and the diagonal band of Broca (o-p and t-u). Dendrites

with long spines (arrowheads) arose from fusiform or triangular-shaped neuronal bodies (arrows), and not differences between *Arg1-Control* and *Arg1-cKO* neurons are evident. Microphotographs a and f are DAPI counterstained to help in the identification of anatomical landmarks. Low magnification l and q microphotographs illustrate the medial septum (squares, m and r) and the diagonal band of Broca (squares, o and t) areas. Scale bars, 1000 μm (a, f, l and q), 100 μm (b, c, g, h, m, o, r, t), and 20 μm (d, e, h, i, n, p, s, u). Data in j and k are in mean \pm s.e.m. Statistical significances were determined by unpaired two-sided t tests. n.s. indicates not significant.

Reporting Summary

Nature Portfolio wishes to improve the reproducibility of the work that we publish. This form provides structure for consistency and transparency in reporting. For further information on Nature Portfolio policies, see our [Editorial Policies](#) and the [Editorial Policy Checklist](#).

Statistics

For all statistical analyses, confirm that the following items are present in the figure legend, table legend, main text, or Methods section.

- | | |
|-------------------------------------|--|
| n/a | Confirmed |
| <input type="checkbox"/> | <input checked="" type="checkbox"/> The exact sample size (n) for each experimental group/condition, given as a discrete number and unit of measurement |
| <input type="checkbox"/> | <input checked="" type="checkbox"/> A statement on whether measurements were taken from distinct samples or whether the same sample was measured repeatedly |
| <input type="checkbox"/> | <input checked="" type="checkbox"/> The statistical test(s) used AND whether they are one- or two-sided
<i>Only common tests should be described solely by name; describe more complex techniques in the Methods section.</i> |
| <input checked="" type="checkbox"/> | <input type="checkbox"/> A description of all covariates tested |
| <input checked="" type="checkbox"/> | <input type="checkbox"/> A description of any assumptions or corrections, such as tests of normality and adjustment for multiple comparisons |
| <input type="checkbox"/> | <input checked="" type="checkbox"/> A full description of the statistical parameters including central tendency (e.g. means) or other basic estimates (e.g. regression coefficient) AND variation (e.g. standard deviation) or associated estimates of uncertainty (e.g. confidence intervals) |
| <input checked="" type="checkbox"/> | <input type="checkbox"/> For null hypothesis testing, the test statistic (e.g. F , t , r) with confidence intervals, effect sizes, degrees of freedom and P value noted
<i>Give P values as exact values whenever suitable.</i> |
| <input checked="" type="checkbox"/> | <input type="checkbox"/> For Bayesian analysis, information on the choice of priors and Markov chain Monte Carlo settings |
| <input type="checkbox"/> | <input checked="" type="checkbox"/> For hierarchical and complex designs, identification of the appropriate level for tests and full reporting of outcomes |
| <input checked="" type="checkbox"/> | <input type="checkbox"/> Estimates of effect sizes (e.g. Cohen's d , Pearson's r), indicating how they were calculated |

Our web collection on [statistics for biologists](#) contains articles on many of the points above.

Software and code

Policy information about [availability of computer code](#)

Data collection

- Imaging: ZEN black 2.3 (Zeiss)
- iDISCO: Operation software of the COLM is built by custom LabView code (PMID: 24945384)
- qPCR: StepOne (ThermoFisher Scientific)
- FACs: FACSDiva™ software (BD Biosciences)
- Behavioral studies: SMART 2.5 (Panlab)
- Electrophysiological recordings: Clampfit 10.2 (Molecular Devices)

Data analysis

- Image analysis and figure assembly: ImageJ/Fiji 1.53t, Photoshop (Adobe), CorelDraw (Corel).
- Electron microscopy: QuPath
- FACS analysis: FACSDiva™ software (BD Biosciences).
- iDISCO: RStudio, MATLAB, TeraStritcher (PMID: 23181553), Amira 3D software (ThermoFisher Scientific), Elastix toolbox (PMID: 19923044, PMID: 24474917), MelastiX MATLAB wrapper (https://github.com/raacampbell/matlab_elastix), Adobe Premiere, GIMP, Inkscape, Microsoft Excel.
- Morphometric analysis (microglia): Microglial tri-dimensional reconstructions were done with a self-customized script (Altivie F, et al.2018). The script was developed with Python 4.5.
- Dendritic spine analysis: ImageJ, Reconstructor (Texas University).
- Basecalling and demultiplexing was performed using Illumina bcl2fastq v2.20.0 software. Reads were aligned to Ensembl GRCm38/mm10 reference genome using STAR v2.6.1d. Gene counts were estimated using featureCounts (v1.5.1). Normalization and sample group comparisons of gene counts were performed using R package DESeq2 (v1.28.1). No filtering was performed prior to sample group comparisons, where the default DESeq2 independent filtering was applied.

- Statistical analysis and graph generation: Prism 8 (v.9.3.1) (GraphPad Software, San Diego, CA, USA) and Stata (v 17.0, StataCorp, College Station, TX, USA).

For manuscripts utilizing custom algorithms or software that are central to the research but not yet described in published literature, software must be made available to editors and reviewers. We strongly encourage code deposition in a community repository (e.g. GitHub). See the Nature Portfolio [guidelines for submitting code & software](#) for further information.

Data

Policy information about [availability of data](#)

All manuscripts must include a [data availability statement](#). This statement should provide the following information, where applicable:

- Accession codes, unique identifiers, or web links for publicly available datasets
- A description of any restrictions on data availability
- For clinical datasets or third party data, please ensure that the statement adheres to our [policy](#)

The data supporting the findings of this study are available within the article, the Supplementary Information files and the Source Data files that accompany this article. RNA-Seq data are deposited in the Gene Expression Omnibus (GSE216893). Any additional data relevant to the manuscript are available from the authors upon request.

Human research participants

Policy information about [studies involving human research participants and Sex and Gender in Research](#).

Reporting on sex and gender	N/A
Population characteristics	N/A
Recruitment	N/A
Ethics oversight	N/A

Note that full information on the approval of the study protocol must also be provided in the manuscript.

Field-specific reporting

Please select the one below that is the best fit for your research. If you are not sure, read the appropriate sections before making your selection.

Life sciences Behavioural & social sciences Ecological, evolutionary & environmental sciences

For a reference copy of the document with all sections, see [nature.com/documents/nr-reporting-summary-flat.pdf](https://www.nature.com/documents/nr-reporting-summary-flat.pdf)

Life sciences study design

All studies must disclose on these points even when the disclosure is negative.

Sample size	No statistical methods were used to predetermine sample sizes, but our sample sizes are similar to those reported in previous publications (PMIDs: 32873805, 30169759, 31006066, 35493109, 26358557, 30104733).
Data exclusions	For behavioural studies we excluded animals without mobility in both groups. This exclusion criteria were pre-established. No other data were excluded from these analyses.
Replication	Data are representative of multiple independent experiments. For each representative image, experiments were performed at least three times with similar results.
Randomization	For behavioural studies, the animals were randomly selected and separated into two groups according to the genotype. In addition, they were subdivided according to gender. For morphometric and manual counting analyses, sample IDs were randomized using randomized numerical ID in Excel (Microsoft).
Blinding	All behavioural studies were blinded including the analysis of the recollected data. For cell manual counting (V.S., R.R., M.C., P.G.R.), morphometric (D.T.), dendritic spine analysis (E.M.P.V.) and electrophysiological analysis (I.M.G.), respective investigators performing the analysis were blinded to the genotypes during data collection.

Reporting for specific materials, systems and methods

Materials & experimental systems

n/a	Included in the study
<input type="checkbox"/>	<input checked="" type="checkbox"/> Antibodies
<input type="checkbox"/>	<input type="checkbox"/> Eukaryotic cell lines
<input type="checkbox"/>	<input type="checkbox"/> Palaeontology and archaeology
<input type="checkbox"/>	<input checked="" type="checkbox"/> Animals and other organisms
<input type="checkbox"/>	<input type="checkbox"/> Clinical data
<input type="checkbox"/>	<input type="checkbox"/> Dual use research of concern

Methods

n/a	Included in the study
<input type="checkbox"/>	<input type="checkbox"/> ChIP-seq
<input type="checkbox"/>	<input checked="" type="checkbox"/> Flow cytometry
<input type="checkbox"/>	<input type="checkbox"/> MRI-based neuroimaging

Antibodies

Antibodies used

- ARG1 (Abcam, ab91279, rabbit polyclonal, Lot#GR3248025-1, GR302764-1); RRID:AB_10674215.
 - ARG1 (SantaCruz, sc-18354, goat polyclonal, Lot#J2015); RRID:AB_2227469.
 - ARG1 (SantaCruz, sc-271430, clone E-2, Lot#B0717); RRID:AB_10648473.
 - CD206 (R&D, AF2535, goat polyclonal, Lot#ABTU0315101); RRID:AB_2063012.
 - CD206-BV421 (Biolegend, 141717, clone C068C2, Lot#B218581); RIDD:AB_2562232.
 - CD68 (Thermo Fisher Scientific, 14-0681-82, rat monoclonal); RIDD:AB_2572857.
 - ChAT (Sigma-Aldrich, MAB5350, mouse); RRID:AB_95218.
 - CLEC7A (Invivogen, #mabg-mdect, rat monoclonal); RRID:AB_2753143.
 - CX3CR1-APC (R&D, FAB5825A, rabbit polyclonal, Lot#ACNQ0313081); RRID:AB_2810937.
 - GALECTIN-3 (R&D, AF1197, goat polyclonal, Lot#JAA0116021); RRID:AB_2234687.
 - GFP (Abcam, ab6673, goat polyclonal, Lot#GR287379-16); RRID:AB_305643.
 - IBA1 (Abcam, ab5076, goat polyclonal, Lot#GR230719-2); RRID:AB_2224402.
 - IBA1 (Wako, 01919741, rabbit polyclonal, Lot#WDE1198); RRID:AB_839504.
 - p75NTR (Promega, G3231, rabbit polyclonal, Lot#0000086012); RRID:AB_430853.
 - Alexa Flour® 488 (A-11055, Thermo Fisher Scientific, donkey anti-goat polyclonal); RIDD:AB_2534102.
 - Alexa Flour® 488 (A-21206, Thermo Fisher Scientific, donkey anti-rabbit polyclonal); RIDD:AB_2535792.
 - Alexa Flour® 555 (A-31572, Thermo Fisher Scientific, donkey anti-rabbit polyclonal); RIDD:AB_162543.
 - Alexa Flour® 568 (A-11057, Thermo Fisher Scientific, donkey anti-goat polyclonal); RIDD:AB_2534104.
 - Alexa Flour® 594 (A-21207, Thermo Fisher Scientific, donkey anti-rabbit polyclonal); RIDD:AB_141637.
 - Alexa Flour® 647 (A-21447, Thermo Fisher Scientific, donkey anti-goat polyclonal); RIDD:AB_2535864.
 - Secondary antibody conjugated to biotin (Vector laboratories, BA-9200, goat-anti mouse); RRID:AB_2336171.
 - Secondary antibody conjugated to biotin (Jackson ImmunoResearch Laboratories, 705-065-003, donkey anti-goat polyclonal); RRID: AB_2340396.

Validation

All antibodies used were validated for use in histological analysis or FACS with mouse samples, which are shown on the website provided by respective companies. Furthermore, we provide number of citations as curated from CiteAb (<https://www.citeab.com/>), Promega (for p75NTR; G3231) and ThermoFisher Scientific (for CD68; 14-0681-82). In addition:

- ARG1 (ab91279, RRID:AB_10674215): 20 citations. This antibody has been validated for this study in IF in Arg1flox/flox;CX3CR1CreER+/- animals, as well as in other applications by others (e.g. WB, PMID: 24224027).
 - ARG1 (sc-18354, RRID:AB_2227469): 12 citations. This antibody has been validated for this study in IF in Arg1flox/flox;CX3CR1CreER+/- animals, as well as in other applications by others (e.g. WB, PMID: 17015747).
 - ARG1 (sc-271430, RRID:AB_10648473): 25 citations. It has been validated by WB (e.g. PMID: 30429607).
 - CD206 (AF2535, RRID:AB_2063012): 47 citations.
 - CD206-BV421 (141717, RRID:AB_2562232): 4 citations. This antibody was validated post-hoc in-house by qPCR and RNAseq.
 - CD68 (14-0681-82, RIDD:AB_2572857): 9 references.
 - ChAT (MAB5350, RRID:AB_95218): 5 citations.
 - CLEC7A (mabg-mdect, RRID:AB_2753143): 14 citations.
 - CX3CR1-APC (FAB5825A, RRID:AB_2810937): 3 citations. This antibody was validated post-hoc in-house by qPCR and RNAseq.
 - GALECTIN-3 (AF1197, RRID:AB_2234687): 15 citations. This antibody has been validated in-house in GAL-3 knockout animals.
 - GFP (ab6673, RRID:AB_305643): 241 citations.
 - IBA1 (ab5076, RRID:AB_2224402): widely used marker for myeloid cells with over 300 citations for immunofluorescence for this reagent in various species including mice.
 - IBA1 (01919741, RRID:AB_839504): widely used marker for myeloid cells with over 300 citations for immunofluorescence for this reagent in various species including mice.
 - p75NTR (G3231, RRID:AB_430853): 15 citations.

Eukaryotic cell lines

Policy information about [cell lines](#) and [Sex and Gender in Research](#)

Cell line source(s)

State the source of each cell line used and the sex of all primary cell lines and cells derived from human participants or vertebrate models.

Authentication	<i>Describe the authentication procedures for each cell line used OR declare that none of the cell lines used were authenticated.</i>
Mycoplasma contamination	<i>Confirm that all cell lines tested negative for mycoplasma contamination OR describe the results of the testing for mycoplasma contamination OR declare that the cell lines were not tested for mycoplasma contamination.</i>
Commonly misidentified lines (See ICLAC register)	<i>Name any commonly misidentified cell lines used in the study and provide a rationale for their use.</i>

Palaeontology and Archaeology

Specimen provenance	<i>Provide provenance information for specimens and describe permits that were obtained for the work (including the name of the issuing authority, the date of issue, and any identifying information). Permits should encompass collection and, where applicable, export.</i>
Specimen deposition	<i>Indicate where the specimens have been deposited to permit free access by other researchers.</i>
Dating methods	<i>If new dates are provided, describe how they were obtained (e.g. collection, storage, sample pretreatment and measurement), where they were obtained (i.e. lab name), the calibration program and the protocol for quality assurance OR state that no new dates are provided.</i>

Tick this box to confirm that the raw and calibrated dates are available in the paper or in Supplementary Information.

Ethics oversight	<i>Identify the organization(s) that approved or provided guidance on the study protocol, OR state that no ethical approval or guidance was required and explain why not.</i>
------------------	---

Note that full information on the approval of the study protocol must also be provided in the manuscript.

Animals and other research organisms

Policy information about [studies involving animals](#); [ARRIVE guidelines](#) recommended for reporting animal research, and [Sex and Gender in Research](#)

Laboratory animals	Mice were used and maintained under a 12-h light/dark cycle at 22–25 °C with access to food and water ad libitum. Mice used in this study: Mus musculus, C57BL/6J (Charles River), P10, P28, P100 females. Mus musculus, C57BL/6J (Charles River), P10, P28, males. Mus musculus, YARG (The Jackson Laboratory, stock # 015857), P10, P13, males. Mus musculus, YARG (The Jackson Laboratory, stock # 015857), P10, P13, females. Mus musculus, CX3CR1-GFP (The Jackson Laboratory, stock # 005582), P10, males. Mus musculus, Arg1flox/flox;CX3CR1CreER+/-, P10, P20, 2 to 3 month-old, females. Mus musculus, Arg1flox/flox;CX3CR1CreER+/-, P10, P20, 2 to 3 month-old, males. Mus musculus, Arg1flox/flox;CX3CR1CreER-/-, P10, P20, 2 to 3 month-old, females. Mus musculus, Arg1flox/flox;CX3CR1CreER-/-, P10, P20, 2 to 3 month-old, males.
Wild animals	This study did not involve wild animals.
Reporting on sex	<i>Indicate if findings apply to only one sex; describe whether sex was considered in study design, methods used for assigning sex. Provide data disaggregated for sex where this information has been collected in the source data as appropriate; provide overall numbers in this Reporting Summary. Please state if this information has not been collected. Report sex-based analyses where performed, justify reasons for lack of sex-based analysis.</i>
Field-collected samples	This study did not involve samples collected from the field.
Ethics oversight	All animal experimental protocols in the present study were in accordance to the respective national, federal and institutional regulations, i.e. the Guidelines of the European Union Council, following Swedish regulations for the use of laboratory animals and approved by the Regional Animal Research Ethical Board, Stockholm, Sweden (Ethical permits N248/13) the Spanish regulations (BOE 34/11370–421, 2013) and in conformity with the Canada Council on Animal Care guidelines.

Note that full information on the approval of the study protocol must also be provided in the manuscript.

Clinical data

Policy information about [clinical studies](#)

All manuscripts should comply with the ICMJE [guidelines for publication of clinical research](#) and a completed [CONSORT checklist](#) must be included with all submissions.

Clinical trial registration	<i>Provide the trial registration number from ClinicalTrials.gov or an equivalent agency.</i>
Study protocol	<i>Note where the full trial protocol can be accessed OR if not available, explain why.</i>
Data collection	<i>Describe the settings and locales of data collection, noting the time periods of recruitment and data collection.</i>

Dual use research of concern

Policy information about [dual use research of concern](#)

Hazards

Could the accidental, deliberate or reckless misuse of agents or technologies generated in the work, or the application of information presented in the manuscript, pose a threat to:

- | No | Yes |
|--------------------------|---|
| <input type="checkbox"/> | <input type="checkbox"/> Public health |
| <input type="checkbox"/> | <input type="checkbox"/> National security |
| <input type="checkbox"/> | <input type="checkbox"/> Crops and/or livestock |
| <input type="checkbox"/> | <input type="checkbox"/> Ecosystems |
| <input type="checkbox"/> | <input type="checkbox"/> Any other significant area |

Experiments of concern

Does the work involve any of these experiments of concern:

- | No | Yes |
|--------------------------|--|
| <input type="checkbox"/> | <input type="checkbox"/> Demonstrate how to render a vaccine ineffective |
| <input type="checkbox"/> | <input type="checkbox"/> Confer resistance to therapeutically useful antibiotics or antiviral agents |
| <input type="checkbox"/> | <input type="checkbox"/> Enhance the virulence of a pathogen or render a nonpathogen virulent |
| <input type="checkbox"/> | <input type="checkbox"/> Increase transmissibility of a pathogen |
| <input type="checkbox"/> | <input type="checkbox"/> Alter the host range of a pathogen |
| <input type="checkbox"/> | <input type="checkbox"/> Enable evasion of diagnostic/detection modalities |
| <input type="checkbox"/> | <input type="checkbox"/> Enable the weaponization of a biological agent or toxin |
| <input type="checkbox"/> | <input type="checkbox"/> Any other potentially harmful combination of experiments and agents |

ChIP-seq

Data deposition

- Confirm that both raw and final processed data have been deposited in a public database such as [GEO](#).
- Confirm that you have deposited or provided access to graph files (e.g. BED files) for the called peaks.

Data access links

May remain private before publication.

For "Initial submission" or "Revised version" documents, provide reviewer access links. For your "Final submission" document, provide a link to the deposited data.

Files in database submission

Provide a list of all files available in the database submission.

Genome browser session

(e.g. [UCSC](#))

Provide a link to an anonymized genome browser session for "Initial submission" and "Revised version" documents only, to enable peer review. Write "no longer applicable" for "Final submission" documents.

Methodology

Replicates

Describe the experimental replicates, specifying number, type and replicate agreement.

Sequencing depth

Describe the sequencing depth for each experiment, providing the total number of reads, uniquely mapped reads, length of reads and whether they were paired- or single-end.

Antibodies

Describe the antibodies used for the ChIP-seq experiments; as applicable, provide supplier name, catalog number, clone name, and lot number.

Peak calling parameters

Specify the command line program and parameters used for read mapping and peak calling, including the ChIP, control and index files used.

Data quality

Describe the methods used to ensure data quality in full detail, including how many peaks are at FDR 5% and above 5-fold enrichment.

Software

Describe the software used to collect and analyze the ChIP-seq data. For custom code that has been deposited into a community repository, provide accession details.

Flow Cytometry

Plots

Confirm that:

- The axis labels state the marker and fluorochrome used (e.g. CD4-FITC).
- The axis scales are clearly visible. Include numbers along axes only for bottom left plot of group (a 'group' is an analysis of identical markers).
- All plots are contour plots with outliers or pseudocolor plots.
- A numerical value for number of cells or percentage (with statistics) is provided.

Methodology

Sample preparation

For RNA-Seq and RT-qPCR, brains were pooled and roughly minced with a scalpel, followed by mechanical dissociation with use of a tissue grinder. The tissue was further homogenized by pipette trituration and passed through cell strainer. Whole-brain homogenate was separated by 20 % Percoll (Percoll PLUS, low endotoxin) gradient centrifugation at 500 g for 20 min at 4 °C (no brake). The pellet was washed and resuspended in cold FACS staining buffer (R&D Systems). Cells were stained with primary antibodies against CX3CR1 (R&D, FAB5825A) and CD206 (Biolegend, 141717) for 45 min at 4 °C.

Instrument

FACSAria III Cell Sorter system.

Software

FACSDiva™ software (BD Biosciences) was used to collect and analyze the data.

Cell population abundance

Post-hoc RNA-Seq data analysis and qPCR confirmed the purity of the samples sorted.

Gating strategy

Gating strategy for this study is shown in Extended Data Fig. 5a. CNS cells were gated (singlets), followed by being gated for CD206 (negative selection), CX3CR1 (positive selection) prior to be divided into ARG1-YFP-positive and ARG1-YFP-negative.

- Tick this box to confirm that a figure exemplifying the gating strategy is provided in the Supplementary Information.

Magnetic resonance imaging

Experimental design

Design type

Indicate task or resting state; event-related or block design.

Design specifications

Specify the number of blocks, trials or experimental units per session and/or subject, and specify the length of each trial or block (if trials are blocked) and interval between trials.

Behavioral performance measures

State number and/or type of variables recorded (e.g. correct button press, response time) and what statistics were used to establish that the subjects were performing the task as expected (e.g. mean, range, and/or standard deviation across subjects).

Acquisition

Imaging type(s)

Specify: functional, structural, diffusion, perfusion.

Field strength

Specify in Tesla

Sequence & imaging parameters

Specify the pulse sequence type (gradient echo, spin echo, etc.), imaging type (EPI, spiral, etc.), field of view, matrix size, slice thickness, orientation and TE/TR/flip angle.

Area of acquisition

State whether a whole brain scan was used OR define the area of acquisition, describing how the region was determined.

Diffusion MRI

Used

Not used

Preprocessing

Preprocessing software

Provide detail on software version and revision number and on specific parameters (model/functions, brain extraction, segmentation, smoothing kernel size, etc.).

Normalization

If data were normalized/standardized, describe the approach(es): specify linear or non-linear and define image types used for transformation OR indicate that data were not normalized and explain rationale for lack of normalization.

Normalization template

Describe the template used for normalization/transformation, specifying subject space or group standardized space (e.g. original Talairach, MNI305, ICBM152) OR indicate that the data were not normalized.

Noise and artifact removal

Describe your procedure(s) for artifact and structured noise removal, specifying motion parameters, tissue signals and

Noise and artifact removal

physiological signals (heart rate, respiration).

Volume censoring

Define your software and/or method and criteria for volume censoring, and state the extent of such censoring.

Statistical modeling & inference

Model type and settings

Specify type (mass univariate, multivariate, RSA, predictive, etc.) and describe essential details of the model at the first and second levels (e.g. fixed, random or mixed effects; drift or auto-correlation).

Effect(s) tested

*Define precise effect in terms of the task or stimulus conditions instead of psychological concepts and indicate whether ANOVA or factorial designs were used.*Specify type of analysis: Whole brain ROI-based BothStatistic type for inference
(See [Eklund et al. 2016](#))*Specify voxel-wise or cluster-wise and report all relevant parameters for cluster-wise methods.*

Correction

Describe the type of correction and how it is obtained for multiple comparisons (e.g. FWE, FDR, permutation or Monte Carlo).

Models & analysis

n/a | Involved in the study

 Functional and/or effective connectivity Graph analysis Multivariate modeling or predictive analysis

Functional and/or effective connectivity

Report the measures of dependence used and the model details (e.g. Pearson correlation, partial correlation, mutual information).

Graph analysis

Report the dependent variable and connectivity measure, specifying weighted graph or binarized graph, subject- or group-level, and the global and/or node summaries used (e.g. clustering coefficient, efficiency, etc.).

Multivariate modeling and predictive analysis

Specify independent variables, features extraction and dimension reduction, model, training and evaluation metrics.